

Time Evolution of 3D Disk Formation with Misaligned Magnetic Field and Rotation Axes

Miikka S. Väisälä^{1,2}, Hsien Shang^{1,2}, Ruben Krasnopolsky^{1,2}, Sheng-Yuan Liu^{1,2}, Ka Ho Lam^{2,3}, and Zhi-Yun Li³

Academia Sinica, Theoretical Institute for Advanced Research in Astrophysics, Taipei, Taiwan; mvaisala@asiaa.sinica.edu.tw, shang@asiaa.sinica.edu.tw

Academia Sinica, Institute of Astronomy and Astrophysics, Taipei, Taiwan

Astronomy Department, University of Virginia, Charlottesville, VA 22904, USA

Received 2018 October 29; revised 2018 December 20; accepted 2018 December 23; published 2019 March 11

Abstract

Distinguishing diagnostic observational signatures produced by MHD models is essential in understanding the physics for the formation of protostellar disks in the Atacama Large Millimeter/submillimeter Array era. Developing suitable tools along with time evolution will facilitate better identification of diagnostic features. With the ray-tracing-based radiative transfer code PERSPECTIVE we explore the time evolution of MHD models carried out in Li et al.—most of which have 90° misalignment between the rotational axis and the magnetic field. Four visible object types can be characterized, origins of which are dependent on the initial conditions. Our results show complex spiraling density, velocity, and polarization structures. The systems are under constant change, but many of those distinctive features are present already early on, and they grow more visible in time, but most could not be identified from the data without examining their change in time. The results suggest that spiraling pseudo-disk structures could function as an effective observation signature of the formation process, and we witness accretion in the disk with eccentric orbits that appear as spiral-like perturbation from simple circular Keplerian orbits. Magnetically aligned polarization appears purely azimuthal in the disk, and the magnetic field can lead to precession of the disk.

Key words: accretion, accretion disks – magnetic fields – magnetohydrodynamics (MHD) – polarization – radiative transfer – stars: formation

Supporting material: animations

1. Introduction

New stars emerge from dense cores within magnetically turbulent molecular clouds, with turbulence originating through a cascade from large scales (mainly driven by supernovae; Korpi et al. 1999). In such a chaotic environment initial conditions for disk formation can be of many different types, one of which is misalignment of rotation and magnetic fields. The recent results from Planck and Herschel illustrate this cascade process better from large to small in our Galaxy. The Planck measurements of foreground polarization (Planck Collaboration et al. 2015a) and their subsequent analysis (Planck Collaboration et al. 2016a, 2016b; Väisälä et al. 2018) have shown how galactic magnetic fields shift from diffuse large-scale turbulent fields to dense giant molecular cloud (GMC) filaments. While the magnetic field appears to have a coherent GMC-scale structure, the polarization fraction is significantly affected by further turbulent fluctuations in the magnetic field (Planck Collaboration et al. 2015b). A follow-up of *Planck* results (Planck Collaboration et al. 2016c), the Herschel Galactic Cold Cores key project (Juvela et al. 2010, 2011, 2012, 2015a, 2015b, 2018; Montillaud et al. 2015; Rivera-Ingraham et al. 2016, 2017) has demonstrated that cold prestellar and starless cores are highly dynamic structures with diverse features. Therefore, the turbulence cascade has a huge influence on protostellar disk formation. The early models of magnetized collapse (e.g., Li & Shu 1996; Tomisaka 2002) assumed highly idealized conditions with simple nonturbulent cores and a neatly aligned rotation axis for reasonable practical purposes. However, the simple models are getting more outdated with the complexity revealed by the Atacama Large Millimeter/submillimeter Array (ALMA), and star formation

theory has to be able to avert the so-called magnetic braking catastrophe.

ALMA has provided extensive observations of objects in the early stages of star formation, namely, the Class 0 stage, which we demonstrate with the following examples. VLA 1623A is a disk system surrounded by a ring (Sadavoy et al. 2018a) showing Keplerian-type rotation (Murillo et al. 2013). Indeed, Harris et al. (2018) have found that there might be two components within the inner part of VLA 1632A. On the other hand, HH 212 is the classical textbook symmetrical disk seen with an equatorial dust lane and well-collimated outflow ejected from the very center of the disk (Lee et al. 2017a, 2017b, 2018). Yet another example is the L1448 IRS3B source, which consists of three protostellar components surrounded by a spiraling density structure (Tobin et al. 2016). In addition, there are objects with X-shaped cavities. Both TMC-1A (Aso et al. 2015; Sakai et al. 2016) and B335 (Yen et al. 2018) have rotating X-shaped envelopes. TMC-1A has been shown to have an aligned velocity gradient with the outflow cavity close to the object center (Bjerkeli et al. 2016), whereas B335 presents coherent magnetization/polarization near the object outflow cavity edges (Maury et al. 2018). The recent observations of IRAS 16293 connect the surrounding magnetic field to a protostellar disk (Liu et al. 2018; Sadavoy et al. 2018b). The systems so far show significant variation in their structures, and understanding them, as well as other objects to be uncovered with ALMA, calls for examining the theoretical and observational implications for more than one model or mechanism. In the case of this study, we look at the observational properties of objects formed with magnetic field and rotation misaligned—one of the proposed solutions to the magnetic braking catastrophe. With such cross-inspection of diagnostic features that can be observed through the input physics, the control process for magnetic braking can be better identified.

In the early days it was assumed that a circumstellar disk would be merely a result of angular momentum conservation of a rotating prestellar core (e.g., Bodenheimer 1995). However, the magnetic field proved to make the matter more complicated. The magnetic braking catastrophe results from accumulation of magnetic flux into the collapse center, in ideal MHD conditions (see Li et al. 2014a; Lizano & Galli 2015, for more extended reviews). When a core collapses, the magnetic field converges toward the center, growing in strength, and during the process the field becomes strong enough to oppose any azimuthal movement (Allen et al. 2003; Galli et al. 2006). This will also lead to overly efficient removal of angular momentum by the outflow, inhibiting disk formation (Hennebelle & Fromang 2008; Mellon & Li 2008). Magnetic braking can also lead to interchange instabilities, disturbing its ordered structure: when the magnetic field is decoupled from the central protostar, some regions around the protostar can grow strong enough to oppose freefall motion (Li & McKee 1996). This phenomenon can produce a system fragmented by so-called decoupling-enabled magnetic structures (DEMSs; Zhao et al. 2011; Krasnopolsky et al. 2012), which appear as low-density, high magnetic field holes around the protostar, which block the rotation of the accretion flow. However, because we know that magnetic protostellar disks exist (Williams & Cieza 2011), something has to make disk formation possible despite the magnetic field.

There are various suggested mechanisms for resolving the magnetic braking catastrophe. They are not contradictory, because in a complete, realistic system all of them could be present in some proportion. However, it is interesting to ask which mechanism dominates and under what conditions. One group of attempted solutions are the non-ideal MHD effects of ohmic resistivity (Dapp & Basu 2010; Krasnopolsky et al. 2010; Machida et al. 2014), ambipolar diffusion (Krasnopolsky & Königl 2002; Mellon & Li 2009; Li et al. 2011), and the Hall effect (Krasnopolsky et al. 2011; Tsukamoto et al. 2017). Non-ideal MHD effects, as long as they are strong enough, would loosen the grip of matter on the magnetic field, thus preventing excessive magnetic braking. However, Krasnopolsky et al. (2012) have demonstrated that non-ideal effects by themselves might not prevent the catastrophe, at least when the canonical level of ambipolar diffusion is adopted.

On the other hand, turbulent diffusion and reconnection of magnetic fields could also make efficient disk formation possible (Santos-Lima et al. 2012; Joos et al. 2013; Li et al. 2014b; Kuffmeier et al. 2017; Matsumoto et al. 2017; Gray et al. 2018). The turbulence studies have provided promising results. Turbulence could create direct diffusion of the magnetic field—particularly in the form of reconnection (Lazarian & Vishniac 1999). Additionally, the turbulent cascade from the large scales could affect the alignment of the magnetic field and the inflow during the star formation process, making it more beneficial for disk formation (Kuffmeier et al. 2017; Gray et al. 2018); this point also connects to the third option, the misalignment of the rotation axis with respect to the magnetic field, which is the specific focus of this study.

There have been a number of studies examining the misalignment (e.g., Machida et al. 2006; Hennebelle & Ciardi 2009; Joos et al. 2012). These studies have shown that

with a mass-to-flux ratio as low as $\lambda\gtrsim 3$ misaligned collapse could produce a rotationally supported disk (RSD). However, a later study by Li et al. (2013, hereafter LKS13) argued that $\lambda\gtrsim 4$ would be the minimum to allow for misaligned disk formation, as their simulation starts from a uniform spherical cloud, whereas earlier models started with a density profile condensed at the center. Therefore, Li et al. (2014a) considered that it would be rare that collapse would have both a misaligned magnetic field and $\lambda\gtrsim 4$, suspecting that a more hybrid approach would be needed to fully resolve the magnetic braking catastrophe.

Since the publication of LKS13, Gray et al. (2018) have explored misalignment with a power-law-scaled initial turbulence starting from a spherical 300 M_{\odot} molecular cloud. They tested two implementations of turbulence: one had the total angular momentum of the turbulence aligned to the magnetic field, whereas the other had it misaligned. They found that aligned turbulence, while leading to efficient star formation, could not produce disks, regardless of the energy of the initial turbulence or levels of mesh refinement. On the other hand, the misaligned turbulence would make disk formation possible, with large-scale cloud rotation/magnetic field misalignment leading to even more star formation. Therefore, Gray et al. (2018) argue that turbulent diffusion, just by itself, cannot fully account for disk formation. They suggest that turbulent misalignment is an essential element of the process. This means that turbulence would, by affecting fluid movements and magnetic field alignment locally, lead to magnetic field alignments over time that would favor disk formation.

In light of the results of Gray et al. (2018), the role of misalignment could be seen as a part of the process related to turbulent collapse at molecular cloud scales. In such a scenario, we will likely find at least some cores for which rotation axis and larger-scale magnetic fields are almost orthogonal to each other—aligned so owing to the influences of larger-scale turbulence. Therefore, it is meaningful to build the basis for observational understanding of such object types.

The series of MHD models, results of which are used as the basis of radiative transfer modeling in this study, were in part presented in LKS13. Of special interest are models G and H, which show signs of disk formation. We use these models to gain insights concerning the observational signatures of the misaligned disk formation process via radiative transfer modeling with key diagnostic elements. We will show that such signatures can be found, and indirect signatures might tell more about the magnetic field than the linear polarization. New understanding of the original MHD models themselves can also be gained. To achieve our aims, we used the simple but efficient radiative transfer code PERSPECTIVE developed within the group to estimate the polarized continuum emission from our model disks along with column density information and position—velocity diagrams.

The rest of the paper is structured as follows. First, we describe the MHD model of LKS13 in Section 2. In Section 3 we describe the basic functionalities of the radiative transfer code PERSPECTIVE and other analysis and fitting methods we have used. In Section 4 we describe general results of the radiative transfer modeling based on LKS13, as well as how we categorize the results by their nature. In Section 5 we discuss what the best observational signatures produced may be, as well as how they are related to the physics and kinematics. We argue that VLA 1623A (Murillo et al. 2013;

Table 1
Models of LKS13 and Their Corresponding Visual Types

Model	λ	θ_0 (deg)	$(10^{17} \text{cm}^2 \text{s}^{-1})$	$M_* \ (M_{\odot})$	Visual Type
A	9.72	0	1	0.24	LP
В	4.86	0	1	0.22	LP
C	2.92	0	1	0.33	LP
D	9.72	45	1	0.21	LP/LS
E	4.86	45	1	0.35	LP
F	2.92	45	1	0.27	LP
G	9.72	90	1	0.38	CS
H	4.86	90	1	0.46	LS
I	2.92	90	1	0.47	LA
M	9.72	90	0	0.10	CS
N	9.72	90	0.1	0.26	CS
P	4.03	90	1	0.32	LS
Q	3.44	90	1	0.22	LA
X	4.00	90	1	0.31	LA
Y	5.00	90	1	0.33	LA/LS
Z	6.00	90	1	0.30	LS

Note. CS: Clear Spiral; LS: Leaking Spiral; LA: Looped Axis; LP: Looped Plane. Boldface highlights the representative model cases featured in the figures.

Murillo & Lai 2013; Harris et al. 2018; Sadavoy et al. 2018a) could be a potential candidate for the misaligned disk formation scenario. Section 6 summarizes the main results.

2. MHD Models

The work presented in this paper has been built on the simulations conducted by LKS13, which aimed to study effects of magnetic field misalignment, particularly in comparison with Joos et al. (2012). LKS13 used a non-uniform spherical grid with a resolution of $96 \times 64 \times 60$ with inner and outer radial boundaries at 10^{14} cm ≈ 6.7 au and 10^{17} cm ≈ 6700 au, respectively. The radial cell size is most resolved near the inner boundary, where $\Delta r = 5 \times 10^{12}$ cm ≈ 0.3 au. The θ -grid is also non-uniform, with higher resolution toward the equator (\sim 0°.63) and lower resolution toward the polar axis (7°.5). For boundary conditions, at the radial boundary, standard outflow conditions were imposed. The azimuthal direction is naturally periodic, and reflective boundaries were imposed at the two polar axes. The mass flowing out of the grid in the inner radial direction accretes to a central point mass.

LKS13 ran the MHD models listed in Table 1. The models started from a sphere with uniform density of $\rho_0=4.77\times 10^{-19}\,\mathrm{g~cm^{-3}}$, radius of $R=10^{17}\,\mathrm{cm}\sim 6700$ au, and solid-body rotation of $\Omega_0=10^{-13}\,\mathrm{s^{-1}}$. Their varied parameters included the mass-to-flux ratio λ , the angle between rotation axis and the magnetic field θ_0 , and degree of ohmic resistivity η . The orientation and strength of the magnetic field were adjusted to get the intended λ and θ_0 with initial field strengths $B_0=10.6, 21.3,$ and $35.4\,\mu\mathrm{G}$. Models P and Q were set to estimate the limit value for λ being able or not to produce an RSD. Models X, Y, and Z had a magnetic field proportional to the column density along each field line.

All models started from ideal MHD, but an explicit small and spatially uniform ohmic resistivity was added after the initial collapse, to avoid numerical instabilities. LKS13 state that added resistivity has little influence on the essential dynamics of their model. The system was governed by a barotropic equation of state, isothermal at low densities and polytropic at high densities. Self-gravity was included, as well as the gravity due to the accreting central point mass.

LKS13 found that the lack of a strong outflow allows the misaligned case to conserve more of the angular momentum, leading to disk formation, unless the system had too strong a magnetic field with $\lambda < 4$. They found that misaligned collapse would be magnetically dominated with rotation approaching Keplerian, and inflow was slower than the freefall velocity. In the process, the magnetic field would wrap itself into a spiraling shape, with adjacent spirals having opposing magnetic polarities.

With aligned collapse or the misaligned case with strong magnetic field, the concentration of magnetic flux near the accreting protostar would lead to the formation of DEMSs (Zhao et al. 2011; Krasnopolsky et al. 2012). DEMSs form when the magnetic pressure around the central object grows strong enough to oppose the ram pressure from the collapse, which will result in areas with low density. The edges surrounding the DEMSs, on the other hand, have enhanced densities, appearing then as loop-like structures.

LKS13 concluded that magnetic misalignment would not be able to explain all disk formation because, according to their estimate, the probability for having favorable conditions for misaligned disk formation would be \sim 12% or less. The likelihood of a suitable condition would be rare. Such an estimate could be, however, too pessimistic. As argued earlier, early protostellar envelopes can have multiple types, for some of which misaligned formation can be relevant. Large-scale turbulence could result in exotic smaller-scale orientations, and Kuffmeier et al. (2017) argue that the mass-to-flux ratio would not be a hard determining feature for the possibility of circumstellar disk formation. In addition, new model results by Gray et al. (2018) demonstrate that magnetic field misalignment can be an important part of the collapse process to some degree. Therefore, modeling observable features of misaligned magnetic field would still be called for so that such behavior could be identified in nature.

3. Methods

MHD models such as those of LKS13 are 3D dynamical entities, and as such their properties can only be fully understood by analysis techniques that take this into account. While LKS13 performed detailed analysis of their physics, apart from some measured quantities, their analysis relied on 2D cutout slices, which, as will be discussed later, miss some essential perspectives on how the system functions in three dimensions and their respective interpretations.

The old analysis could address the observational implication only in a limited way, which is a matter that requires extended consideration. Therefore, to deepen the original work, we aimed to examine the LKS13 data like observable objects. This would mean doing simple radiative transfer modeling of column density, polarization, and projected physical quantities like velocity—with a large collection of MHD model frames.

A simple ray-tracing code PERSPECTIVE was built for such a purpose, and this is the first time that the code has been used in a scientific study. PERSPECTIVE is capable of integrating the above-listed quantities from a chosen viewing angle producing

estimates for observations. Due to its flexibility and efficiency, it can be also treated as a data-viewing tool. In this section we introduce its basic functioning and further data analysis methods.

3.1. Ray Tracing and Polarization

PERSPECTIVE calculates radiative transfer with a ray-tracing method. To do so, PERSPECTIVE pre-calculates all paths of the rays across the examined computation volume, performing relevant interpolations along the way, based on the ZeusTW data cube and a choice of viewing angles and zoom levels. After determining and interpolating the rays, the gas column densities can be integrated along the line of sight (LOS) with

$$\Sigma = \int \rho \, ds,\tag{1}$$

where ρ is the gas density, ds is the LOS length differential, and the integration is computed along the whole length of the ray.

PERSPECTIVE is able to calculate the Stokes parameters of emitted polarization based on the method presented by Fiege & Pudritz (2000), assuming an optically thin medium. Therefore, the polarization parameters q and u are obtained by integrating the rays along the LOS as

$$q = \int \rho \cos 2\psi \cos^2 \gamma \, ds \tag{2}$$

$$u = \int \rho \sin 2\psi \cos^2 \gamma \, ds,\tag{3}$$

where γ is the angle between the plane of the sky (POS) and the local direction of the magnetic field, and ψ measures the direction of the local polarization angle tilted 90° from the projected POS magnetic field direction within the given integration element.

In addition, we get the magnetic structure parameter

$$\Sigma_2 = \int \rho \left(\frac{\cos^2 \gamma}{2} - \frac{1}{3} \right) ds. \tag{4}$$

From these an estimate of polarization fraction p can be calculated by using

$$p = \langle \alpha \rangle \frac{\sqrt{q^2 + u^2}}{\sum -\langle \alpha \rangle \Sigma_2},\tag{5}$$

where we assume $\langle \alpha \rangle = 0.1$ as in Fiege & Pudritz (2000). This is an approximate observationally estimated scaling factor, and our analysis will avoid relying on the absolute values of p and focus more on its variation. Stokes I,Q, and U are presented in computer units for the sake of simplicity, as in our analysis only relative values have meaning. The scaling of the units assumes a single dust species and a constant dust temperature with related coefficients scaled to unity. In addition, dust alignment efficiency and gas-to-dust relation are kept constant. See Fiege & Pudritz (2000) for the use of this model under wider assumptions.

While the method is simple, it is efficient when calculating Stokes parameters from all of the hundreds of MHD model frames from multiple perspectives. The method connects polarization directly with the magnetic field geometry.

However, our approach does not account for other mechanisms affecting polarized emission, such as self-scattering from thermal emission (Kataoka et al. 2015; Yang et al. 2016), or if dust grains are directly aligned by the radiative flux from the central protostar itself (Tazaki et al. 2017). In addition, we are not performing our analysis with multiple dust species. Therefore, our polarization results are related only to an object's density and magnetic field geometry. This is a practical approach because magnetic alignment is straightforward to compute with the PERSPECTIVE method, while other mechanisms would require a more complex, and therefore more computationally heavy, approach, suitable only to a small number of MHD model frames. Because there is not yet complete consensus on the impact of all these polarization mechanisms, estimates of the magnetic alignment effect can still be very informative in understanding its potential role.

In addition to the polarized emission, we have calculated other derived values described in detail in the Appendix. These include LOS velocity averages for all Cartesian components $v_{\rm LOS}$, $v_{\rm W}$, and $v_{\rm N}$ —or LOS, west, and north directional velocities, respectively. In addition, disk height H_z , disk tilt angle ξ , apparent momentum $p_{\rm mom}$, and average peak location ζ are calculated based on a Gaussian fit.

4. Results

With the methods presented above, we produced hundreds of images. Because it would be impossible to show all of them, we have to focus on highlights and generalized descriptions. Fortunately, we have found that certain basic elements stay fairly consistent, and we can present a simplified four-type categorization for the majority of the results.

For the results to be helpful for observational interpretation, there is a need to be able to clearly differentiate the types of objects produced by the MHD modeling in reasonable categories that are based on their visual nature. Looking that way, essentially four different special object types can be seen from the results. These fairly well represent what LKS13 described as "robust" and "porous" RSDs, but they aim to be more descriptive from an observational standpoint.

These categories are arbitrarily named *Clear Spiral*, *Leaking Spiral*, *Looped Axis*, and *Looped Plane*:

- 1. Clear Spiral (CS) shows a distinctive spiral-like shape, which is visible in both the column densities and the observed polarization. However, no outflows are visible, and no axial infall streams can be seen from column densities.
- 2. Leaking Spiral (LS) is similar to the CS, but the system shows clear signs of precession of the disk plane and of the axial infall stream ("infunnel"), which is visible as a cone-like shape in column densities, with some sporadic outflows. Both the CS and LS cases show a two-armed spiral-like pseudo-disk.
- 3. *Looped Axis (LA)* type object shows horizontal, growing loop-like features identified as DEMSs with magnetic braking preventing disk formation. An arched bar-shaped pseudo-disk is visible face-on.
- 4. Looped Plane (LP) is a system that forms DEMS loops near the rotational plane, with magnetic braking preventing disk formation. There is a flat pseudo-disk but no disk.

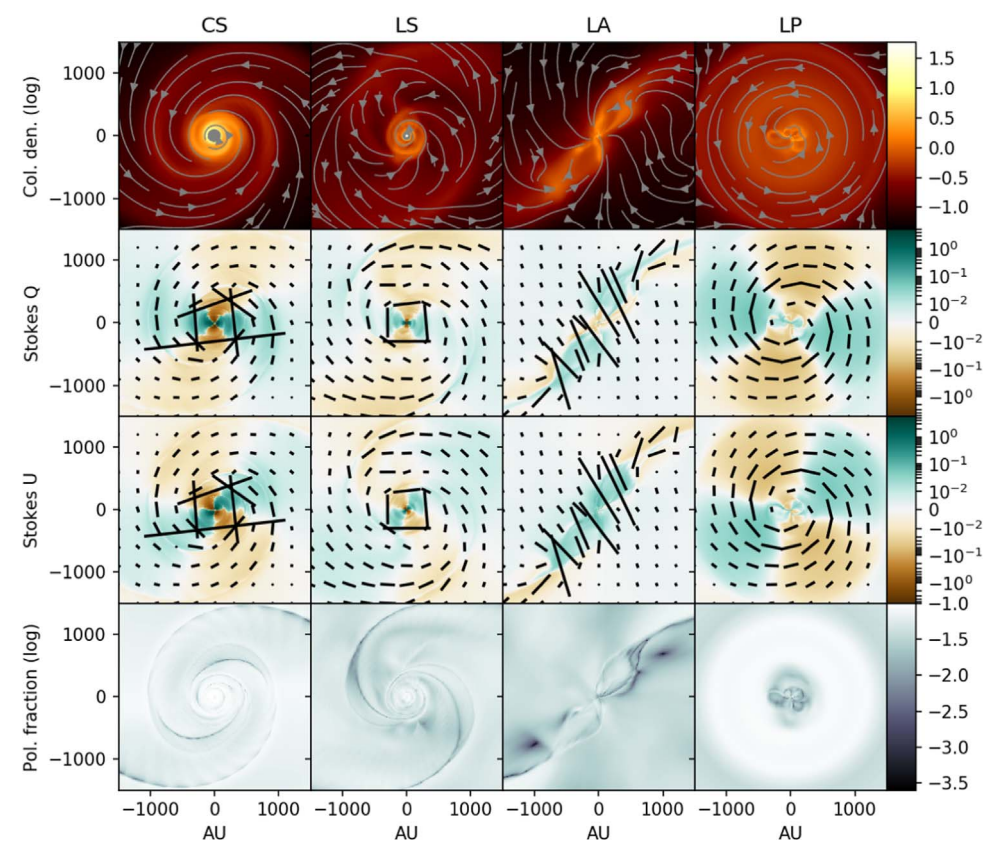


Figure 1. Models G (CS-type), H (LS-type), I (LA-type), and A (LP-type) viewed from above (large scale). The streamlines on the column density maps show the direction of flows along the picture frame. The black lines over Stokes Q and U parameters depict the direction of magnetic field estimated from the polarization angles ("B-vectors"), the length of which is scaled according to the polarized intensity ($\sqrt{Q^2 + U^2}$) of the given frame. (An animation of this figure is available.)

For visual samples of these object types, see Figures 1–6. Table 1 groups the physical models with the visual types. These essentially contain all of the produced object types in a clear-cut manner. Exceptions would be models D and Y, which very much resemble the LS case but are weaker than the others.

Model D resembles model A in many respects, as DEMSs are clearly visible in its rotational plane, lacking the coherent disk-like surface structure of models G and H, however resembling them in the outer parts of the system. However, model D is more disk-like than model A, and LKS13 classified it as a "porous" disk. Because PERSPECTIVE results do not present a convincing and persistent disk, we have decided not to give it a special category in our discussion. Regardless, a particular feature of model D is its surrounding pseudo-disk, oriented along the 45° angle of the magnetic field. Model Y, classified as a "porous disk" by LKS13, resembles an LA case but shows a weak indication of a disk-like structure with no precession, making it another boundary case in the set of models

Within the models under the stated categories there can still be physical differences. However, the differences are so fine that they do not produce distinctively different observational features. Therefore, most of the time we focus on the representative case for each category, which are models **G**, **H**, **I**, and **A**, respectively (Table 1).

The four categories are related to their characteristic initial conditions, which can be reduced to the relative orientation of the magnetic field and its strength. Table 2 lists the basic initial conditions leading to each visual type. The "weak field" refers

 Table 2

 Reference Table for Corresponding Visual Types with Initial Conditions

Visual Type	Initial Conditions
Clear Spiral (CS)	Misaligned weak field
Leaking Spiral (LS)	Misaligned medium field
Looped Axis (LA)	Misaligned strong field
Looped Plane (LP)	Aligned field of any strength

to a mass-to-flux ratio (λ) of 9.72, in LKS13. The "medium field" corresponds to $\lambda = 4.03$ –4.86 and the "strong field" to $\lambda = 2.92$ –3.44, if we list only misaligned collapse cases that started from an initially uniform magnetic field.

The misalignment of rotation and magnetic field has a significant dynamical importance, beyond the strength of the field itself. With the misaligned magnetic field, the strength of the field itself is of dynamical importance. While the strong case prevents it, the medium and weak fields lead to disk formation.

When examining these objects, two approximate scales are helpful. $R \sim 1000\,\mathrm{au}$ scales give a sense of the whole model object. This especially highlights the features relating to the surrounding envelope, as some of the particularities relate to the infall from the envelope. On the other hand, $R \sim 100\,\mathrm{au}$ looks into the inner part, where the CS and LS cases form an early disk. Let us look first at large scales.

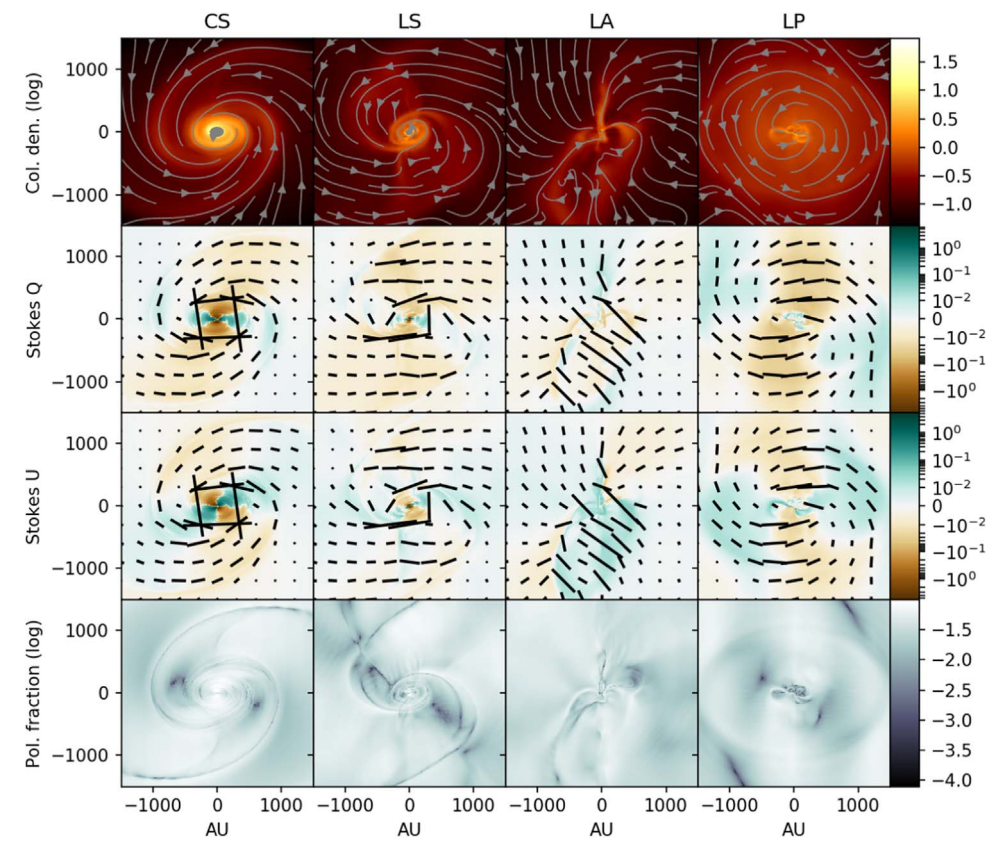


Figure 2. Models G (CS-type), H (LS-type), I (LA-type), and A (LP-type) viewed from a 45° angle (large scale). (An animation of this figure is available.)

4.1. Large Scales ($R \sim 1000 \ au$)

In the CS case, by the end of the MHD simulation, viewed from above, the system has formed a two-armed spiral-like shape that is relatively regular (see Figure 1), although the inner region is more tangled than the outer region. This appearance can be still perceived from 45° inclination (see Figure 2). Looking edge-on, there are no visible outflows, and the inner disk is surrounded be an almost symmetric shell (see Figure 3). However, the velocity analysis shows that there are inflows in both the polar and plane-wise directions, discussed more in Section 4.6. The inflows follow the spiral ridges.

Dynamically the outer and inner spirals of the CS case behave differently. The shape of the outer spiral remains relatively stable in time, but the rapidly rotating inner spiral shows oscillatory modes where spiral arms are no longer clearly distinct. In later frames of the model G simulation, we see that a blob on that inner spiral becomes super-Keplerian and momentarily finds a higher orbit along the rotational plane before rejoining the spiral inflow. This is shown in the bottom left panel of Figure 7, and the Gaussian fit analysis of the oscillations is presented in Section 4.5.

An LS object (model H) has very similar characteristics to the CS case, but the system is more irregular, with smaller and less dense disk. Of particular note is that the rotational plane of the system is tilted owing to precession and a cone-like funnel-shaped axial infall structure is witnessed, which we call for short an *axial infunnel*, coining a natural and useful term if it does not already exist. While the bulk of the accretion is concentrated on the disk plane, the effects of axial inflow are

strong enough to be noticeable. A funnel-shaped infall can also be found in the CS case, when velocities are examined, but it has no clearly visible correspondence in the column densities.

The infunnel witnessed in the LS case is irregular and shows variation of shape and size over time, making it especially apparent in movement (see Figure 8). Looking at small scales, some precession along with the disk is noticeable (see Figures 8, 9, and 10). The infunnel can look deceptively like a conical outflow structure, due to its visual shape and alignment with the disk; however, when actual flow lines are displayed, the direction of the flow toward the central core is clear. The outflow in the LS case is only sporadic and noncontinuous. However, outflow ejection does open up the infunnel, likely due to the release of magnetic energy. This axial infunnel is further discussed in Section 5.3.

The other cases, however, do not form a spiral-like end state, or a disk. LA objects have DEMS-like empty areas with loop-like edges extending outward along the rotational axis from the central point. Viewed face-on, an arched bar-like pseudo-disk is visible, with an X-shaped ridge around the central object, lacking a disk. LP cases have similar effects, where the growing magnetic instability leads into development of DEMSs with their loop-like edges. In motion, the DEMSs circulate around to the rotational plane of the system with one edge facing the central object. Increased initial magnetic field makes these edges of DEMSs more stable and thick, and the DEMSs appear as even more visible holes in the density structure. LA and LP cases display wide continuous outflows, with LA along the rotation axis and LP in the rotational plane perpendicularly to the initial magnetic field direction. Both are connected to the

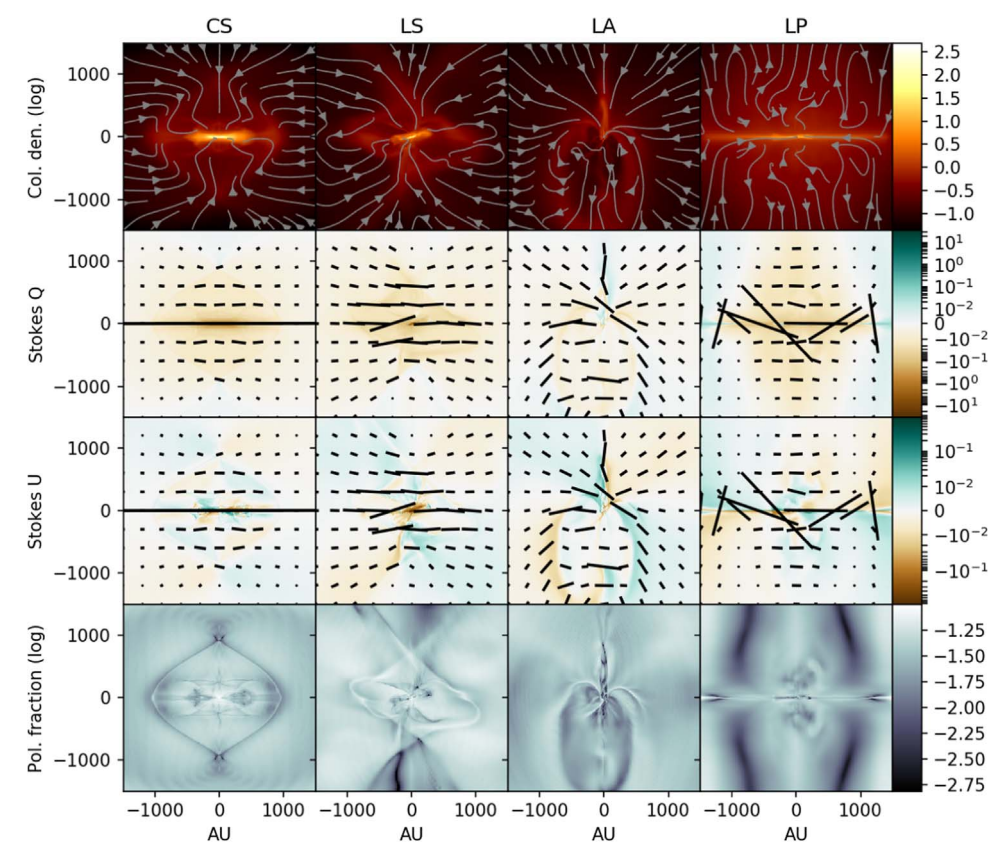


Figure 3. Models G (CS-type), H (LS-type), I (LA-type), and A (LP-type) viewed edge-on (large scale). (An animation of this figure is available.)

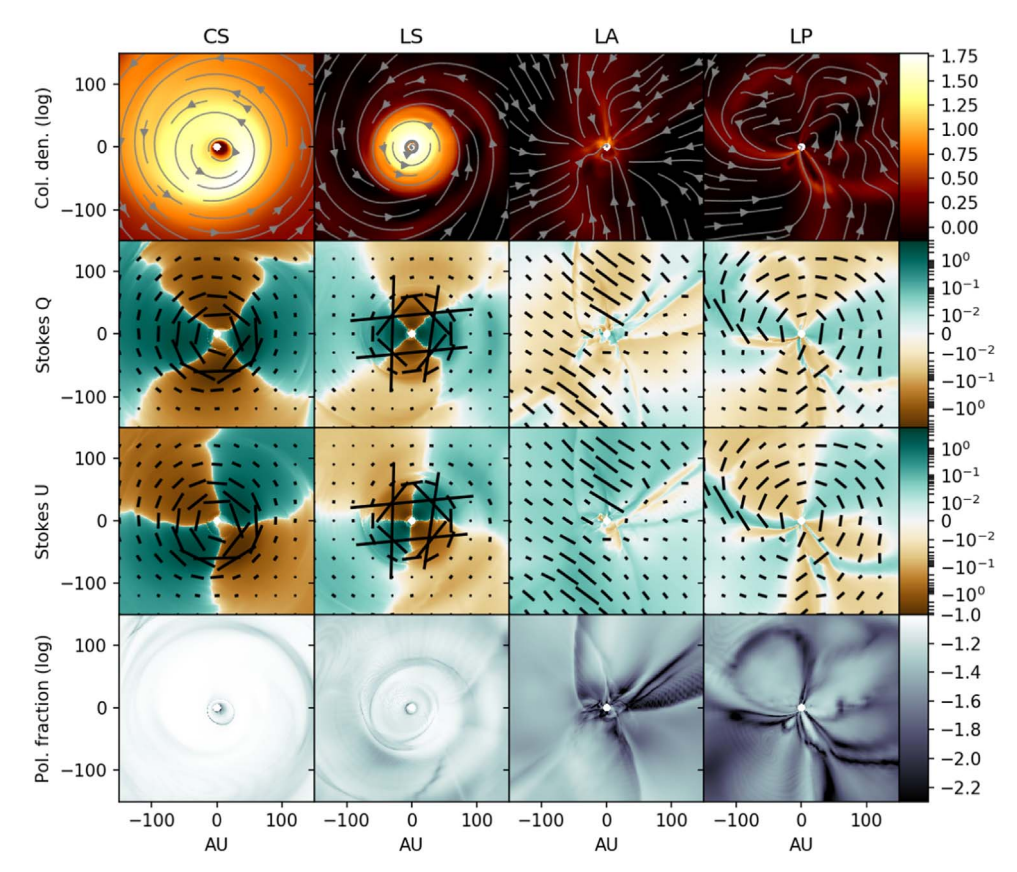


Figure 4. Models G (CS-type), H (LS-type), I (LA-type), and A (LP-type) viewed from above (small scale). (An animation of this figure is available.)

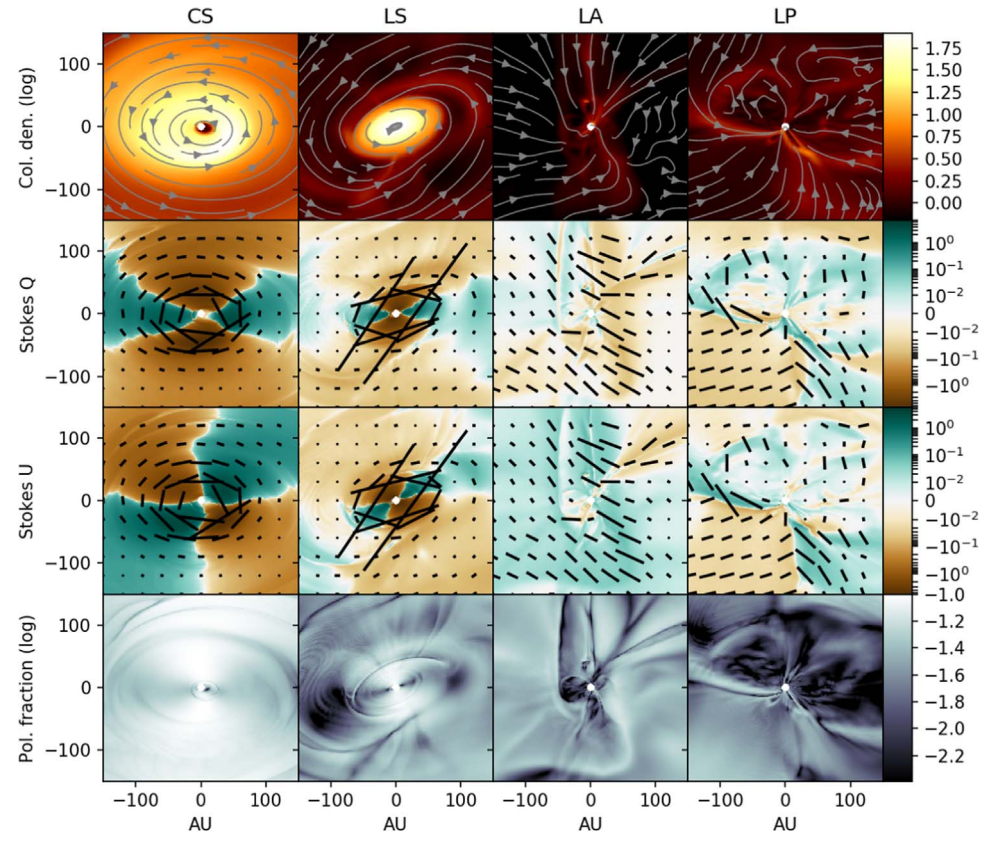


Figure 5. Models G (CS-type), H (LS-type), I (LA-type), and A (LP-type) viewed from a 45° angle (small scale). (An animation of this figure is available.)

excessive magnetic braking. The ambiguous case with 45° misalignment, model D, shows LP-like outflow behavior.

In LP and LA cases there is no disk formed in the end. Due to the lack of disk formation, most of the further analysis in this paper will focus on the CS and LS cases, for which most of the more detailed analysis is more functional and appropriate within the scope of this study.

4.2. Small Scales ($R \sim 100 \ au$)

What makes the small scales noteworthy is the formation of a disk-like object at the center of the system in the CS and LS cases (see Figures 4–6). The disk in the CS case is approximately 200 au in diameter and retains a spiral structure. In contrast, the 100 au diameter disk in the LS case is precessing around the rotation axis, which is the likely reason why its existence was not properly detected by LKS13, which relied on cutout slices from the model frames. A close-up of LS precession is demonstrated in Figure 9. In the CS case, the disk has no visible precession during its whole development (see also Section 4.5), and the inner spirals of the disk wrap themselves around tightly.

The LS case displays additional curious behavior: the disk often contains two differently precessing components—best noticed when the object is observed in movement. The outer ring forms a band, which then precedes around the central protostar. The inner ring is denser than the outer ring, and it precedes around the center with a slightly faster frequency than the outer ring. The bottom left panel of Figure 9 demonstrates that occasionally a gap appears between the two rings. The

inner and outer components are visible in models H and P, but not in model Z.

In short, the CS case displays a larger disk 200 au in diameter without visible precession, while the LS case has a smaller 100 au disk, which shows steady precession over time. There is a noticeable jump in column density between the disks and their surroundings, and it is therefore reasonable to consider the disks to be distinct objects embedded within the rest of the system. This jump has been clearly detected in, e.g., HH 212 (Lee et al. 2017b). This strengthens the case for using high-resolution dust continuum imaging to detect disks in protostellar systems.

4.3. Polarization Characteristics

Polarization calculated with PERSPECTIVE is directly connected to the magnetic field. Looking at Figures 4–6, the contrast between the disks and their surroundings in polarization is strong. This was to be expected, because both CS and LS disks wrap a strong azimuthal magnetic field around themselves. Therefore, Stokes Q and U appear regular in the CS and LS cases, where most of the polarized emission is focused on the dense disk.

In the LP and LA cases irregularities are visible surrounding the DEMSs; because magnetic pressure is strong, and a large part of the angular momentum is lost, the field no longer strictly follows a geometry driven by rotation. However, additionally noteworthy is the hourglass pattern seen in the LA case from above (Figure 1), likely signifying the rigid behavior of the magnetic field in the large scales. In CS and LS systems, viewed from above (Figure 2), the spiral structure can be traced

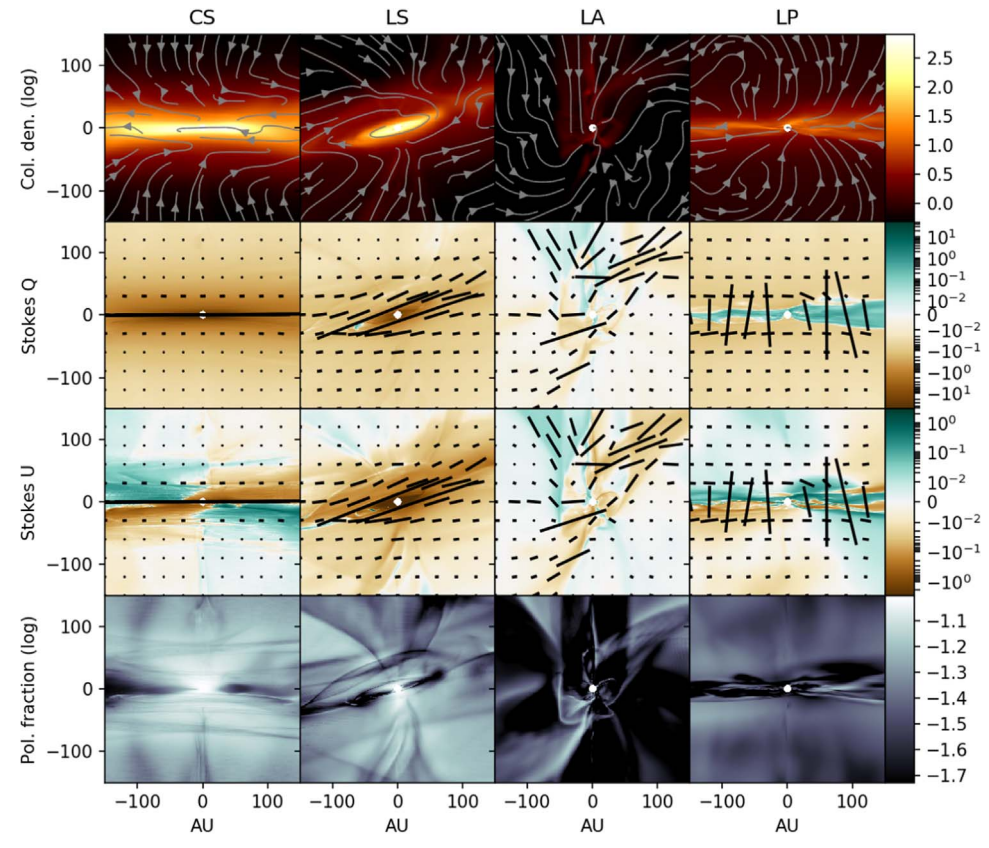


Figure 6. Models G (CS-type), H (LS-type), I (LA-type), and A (LP-type) viewed edge-on (small scale). (An animation of this figure is available.)

corresponding to where the polarization degree is weak. Also, the polarization-derived *B-vectors* show hints of spiral geometry. The inner disk inherits the spiral-like nature of the system, but that is only weakly noticeable in polarization (Figure 5). These features might not remain noticeable, however, because spiral features are mostly visible in connection to the inflow envelope around the disk, where, as will discussed in Section 4.4, the effect will be muddled by noise.

The polarization behavior of LS resembles that of CS. However, the geometry is more irregular, with the disk being smaller and therefore having smaller surface area where the polarization is coherent. The RSD shows a new feature: that polarization is connected to the precession of the disk. The precession is reflected in the polarization, with B-vectors being aligned in the disk plane (Figure 6).

In both CS and LS cases B-vectors show a clear toroidal field direction when observed edge-on, in that they present a similar kind of orientation to a typical edge-on disk (see, e.g., Lee et al. 2018, for a recent dust polarization observation of HH 212), or the surrounding pseudo-disk. Therefore, observation of B-vectors will not differentiate the misaligned disk formation from more ordinary scenarios.

In LP polarization shows rotational characteristics, but growing in irregularity toward the center. When DEMSs form, polarization follows the edges of the DEMSs, tracing their borders. The DEMSs can only be perceived from above, with B-vectors following azimuthal direction. It is noteworthy that the LP case shows B-vectors with apparently poloidal alignment in the small scale (Figure 6), while the outflow

displays toroidal B-vectors (Figure 3). With LA, near the vertical DEMS edge-like loops there is the strongest variation in polarization parameters. Seen from above, the LA has B-vectors perpendicular to the bar-like density structure.

4.4. Effects of Instrument Resolution

Having characterized the properties of our object types, the question remains, how do limited resolution and signal-to-noise ratio (S/N) affect the results? Many features seen by PERSPECTIVE can be muddled by telescope beam and sensitivity; therefore, consideration for instrument limits is called for. Let us assume that the object would be relatively close by, at a distance of 120 pc, and that the resolution corresponds to 0."25 (as in the observation of VLA 1623A by Sadavoy et al. 2018a).

Let us then divide this into four levels of S/N: 10, 100, 500, and 1000. In this case S/N is determined as for Stokes I, Q, U as

$$S/N = \frac{\max(I_{CS})}{\sigma_I},$$
 (6)

$$S/N = \frac{\max(|Q_{CS}|, |U_{CS}|)}{\sigma_{QU}}.$$
 (7)

The fluctuations are scaled with the values of CS (model G), so that the noise level is similar in every case. In addition, both Q and U share the same level of noise. The noise itself is assumed to follow a Gaussian distribution. In addition, based on the determined σ_{QU} , we also calculate a basic maximum likelihood debiased polarized intensity (Simmons & Stewart 1985;

S/N	CS	LS	LA	DL
8	CO, PS	CO		
16	CO, PS	CO	•••	
32	DLO, PS	CO, PS		
64	DLO, SS, PS	CO, PS		
128	DLO, SS, PS	DLO, DI, PS		
256	DLO, SS, PS	DLO, SS, DI, PS	Bar, DEMS	DEMS
512	DLO, SS, PS	DLO, SS, DI, PS	Bar, DEMS	DEMS
1024	DLO, SS, PS	DLO, SS, DI, PS	Bar, DEMS	DEMS

Note. CO = compact object; DLO = disk-like object; SS = spiral structure; PS = polarized structure; DI = disk inclination.

Vaillancourt 2006),

$$\mathcal{P}_I = \sqrt{Q^2 + U^2 - \sigma_{QU}^2},\tag{8}$$

and we mark the regions with $\mathcal{P}_I \leq 1\sigma_{QU}$ and $\mathcal{P}_I \leq 4\sigma_{QU}$ in Figures 11–13 to compare with Sadavoy et al. (2018a).

Some object types are clearly more visible with regard to instrument sensitivity (see Table 3). A CS object is the most coherent and visible. LA and LP cases require the highest sensitivity. In principle, this would mean that the disk and some of the surrounding inflow formed in the misaligned magnetic field situation should be resolved, and even some of the spiral characteristics should be visible. However, if the system is closer to the LS case, all the features become more difficult to recognize, because the LS disk is less dense and coherent, with a smaller diameter.

DEMSs are not likely observable, as they require high sensitivity to be seen. Considering also the loss of extended emission in interferometric observations, it would be highly unlikely that the edges of DEMSs could be distinguished from other kinds of filament-like irregularities, lacking sufficient contrast.

In more specific cases, to approximate the sensitivity of Sadavoy et al. (2018a), we get $S/N \sim 1000$ for I and $S/N \sim 50$ for Q and U. Results are shown in Figures 11–13. It seems, therefore, that the corresponding ALMA resolution and sensitivity should be in principle enough to recognize traces of the spiraling gas, not counting complexities caused by interferometry. However, polarization itself would only give an impression of a simple toroidal magnetic field at best, with noise making any spiral geometry practically invisible.

4.5. Time Development: Gaussian Analysis

Following the methods described in Appendix A.2, we get some results describing the characteristic behavior of the system. We have left out the LA- and LP-type systems from this analysis. Those do not produce a disk—making the Gaussian fitting method unreasonable.

In all cases, after a visible disk-like object has emerged from the initial envelope, essentially when there is enough mass in the central protostar to be gravitationally significant, the scale height remains around an approximate average value, and these averages range between $H_z \sim 5$ and ~ 20 au for model H and are at $H_z \sim 6$ au for model G (see Figure 14, Top). The higher variability of model H is most likely due to its precession, which changes its apparent width somewhat with regard to the

fitting method. As will be discussed in Section 5.1, the magnetic field might be a reason for such a stable scale height.

Model G does not show any kind of tilting, the disk being almost perfectly aligned with the horizontal direction for the duration of the whole simulation (see Figure 14, middle panel). However, model H shows clear precession, with a precession angle of $\xi \sim 20^{\circ}$ when the system is most coherent toward the end, and the timescale of a single round of precession is $\sim 30 \, \text{kyr}$. When observed in motion, the precession is obvious as soon as a resemblance of a disk is seen.

In the bottom panel of Figure 14 we display the change of apparent momentum $p_{\rm mom}$ over time. In model G, after initial growth the momentum decreases, with the strong changes reflecting the moments when mass is absorbed by the central object, therefore disappearing from the disk itself. The irregularities in model H might be partially due to the projection effects caused by precession. However, in general the model G object has more momentum, reflecting the stronger magnetic braking in model H (LKS13).

Figure 15 displays fitted $I_{\max,i}$ as a function of time for model G, as an example. These can be reflective on the oscillation of spirals, specifically their projection. In the top panel of Figure 16, the mean peak location ζ is traced, showing for model G a pattern of oscillations, not seen in the case of model H. This is likely a combination of effects from both wrapping up of magnetic field lines and self-gravity. To make this clearer, we took a standard Lomb-Scargle periodogram of ζ , getting the bottom panel of Figure 16. A Lomb-Scargle periodogram is a common method of calculating power-spectra of an unevenly spaced time series within a set range of periods (Lomb 1976; Scargle 1982). Model G shows a peak at $T \sim 7.5$ kyr, with a smaller peak between $T \sim 2.5$ and 5 kyr. As such, this would support the visual observation that the spiraling disk has several shorter and longer oscillatory modes with regards to its orbital motion as discussed in the Section 4.1. Model H shows comparable behavior to the main peak at $T \sim 10$ kyr and a smaller peak found in a similar range to model G. However, ζ is less clearly resolved.

4.6. Velocity

LKS13 found model G to produce an RSD, and we would add model H to the list, both corresponding to what we call here CS- and LS-type objects. While PERSPECTIVE is not capable of genuinely simulating radial velocities measured from the spectral lines, we can still explore how flows within the core relate to what is visualized.

As described in Appendix A.1, we calculated the density-weighted LOS averages of all Cartesian velocity components. As radial velocities $v_{\rm LOS}$ are what in principle could be directly observed, we constructed a position–velocity (PV) diagram for the edge-on models using the horizontal axis equivalent to the numerical midplane. Figure 17 shows the PV diagrams of models H and G, and in both cases their rotational profile is fairly similar.

The velocity profile with a Keplerian power-law index,

$$v_{\rm kep} = \sqrt{\frac{2GM_*}{R}},\tag{9}$$

is calculated based on the mass of the central point (M_*) . As can be seen, the fastest velocities in the distribution, which trace best the rotating disk velocities, approach Keplerian,

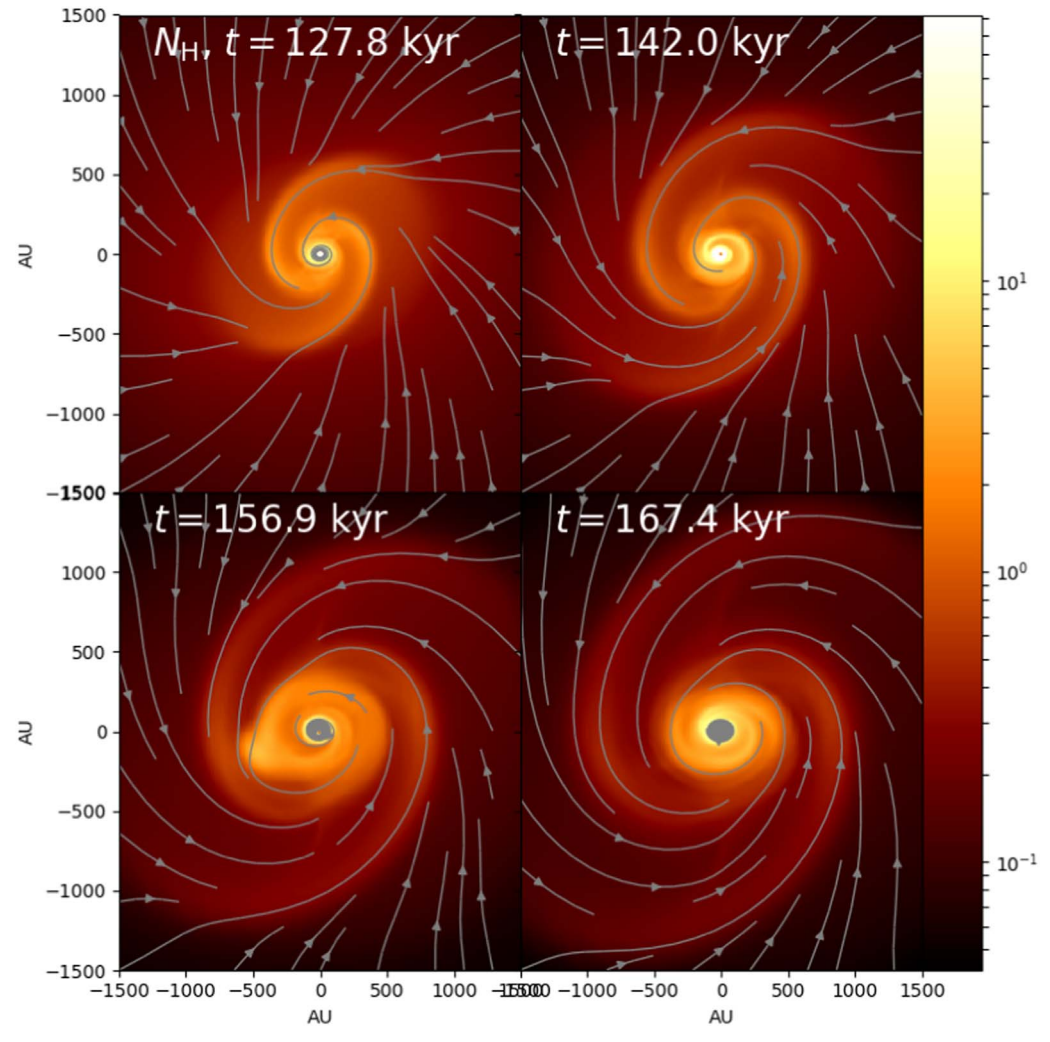


Figure 7. Time development of model G (CS case), viewed from a 45° angle. The colors refer to column densities.

where the curve behaves approximately, but not absolutely, as an upper limit. Therefore, the disks are not strictly Keplerian, with respect to the central point mass, with the spiral structures in particular leading to systematic deviation from circular Keplerian velocity, discussed more below.

To explore non-Keplerian disk behavior, we analyzed the relative deviation from Keplerian power law, based on the analysis of Teague et al. (2018). Therefore, we calculate $\delta v_{\rm rot}$ with

$$\delta v_{\rm rot} = \frac{v_{\rm rot} - v_{\rm kep}}{v_{\rm kep}} \tag{10}$$

based on the LOS velocity averages and assuming that the system rotates around the central point mass in a counter-clockwise direction. $v_{\rm kep}$ is cylindrically symmetric, lacking eccentricity in its orbital direction. We denote $v_{\rm rot} < v_{\rm kep}$ as "sub-Keplerian" and $v_{\rm rot} > v_{\rm kep}$ as "super-Keplerian" motions. The result for models G and H are shown in Figure 18. We can see that only the spiral ridges in the velocity patterns have rotational velocities approaching the corresponding circular Keplerian velocity, and at some points (e.g., parts of the inner disk of model G) $v_{\rm rot}$ can be even faster than $v_{\rm kep}$ itself (leading to the transient orbiting behavior discussed in Section 4.1).

Therefore, magnetic forces and self-gravity contribute to the rotational velocities of the model disk in significant ways, both enhancing and restricting it. Seen edge-on, we see torus-like quasi-Keplerian regions that correspond to the visible projection of the spirals.

The development of $\delta \nu_{rot}$ in time is described in Figure 19, with the rms values ($\langle \delta \nu_{rot} \rangle$) calculated from $\delta \nu_{rot}$ maps, viewed from the top like in Figure 18. The value of $\langle \delta \nu_{rot} \rangle$ does not change considerably from the beginning. The quick variation of $\langle \delta \nu_{rot} \rangle$ in model G corresponds to the occasionally rapid mass accumulation by the central object. Considering also the difference in the magnetic field strengths, the stronger field leads to larger difference from circular Keplerian velocities with respect to the central mass.

In Figure 18, we also show the POS streamlines for the flows in the system. While these cannot be directly observed without sufficient inclination based on radial velocities, they reveal a notable pattern in the inflow in relation to rotation. First, due to magnetic forces around 1000 au radius, the horizontal inflow drops in a $\sim 90^\circ$ angle toward the midplane. Second, the flow spirals downward toward the central mass along the horizontal plane, forming a pattern of accretion. These features can be best understood by looking into the phenomenon of the pseudodisk, which will be further examined in Section 5.1.

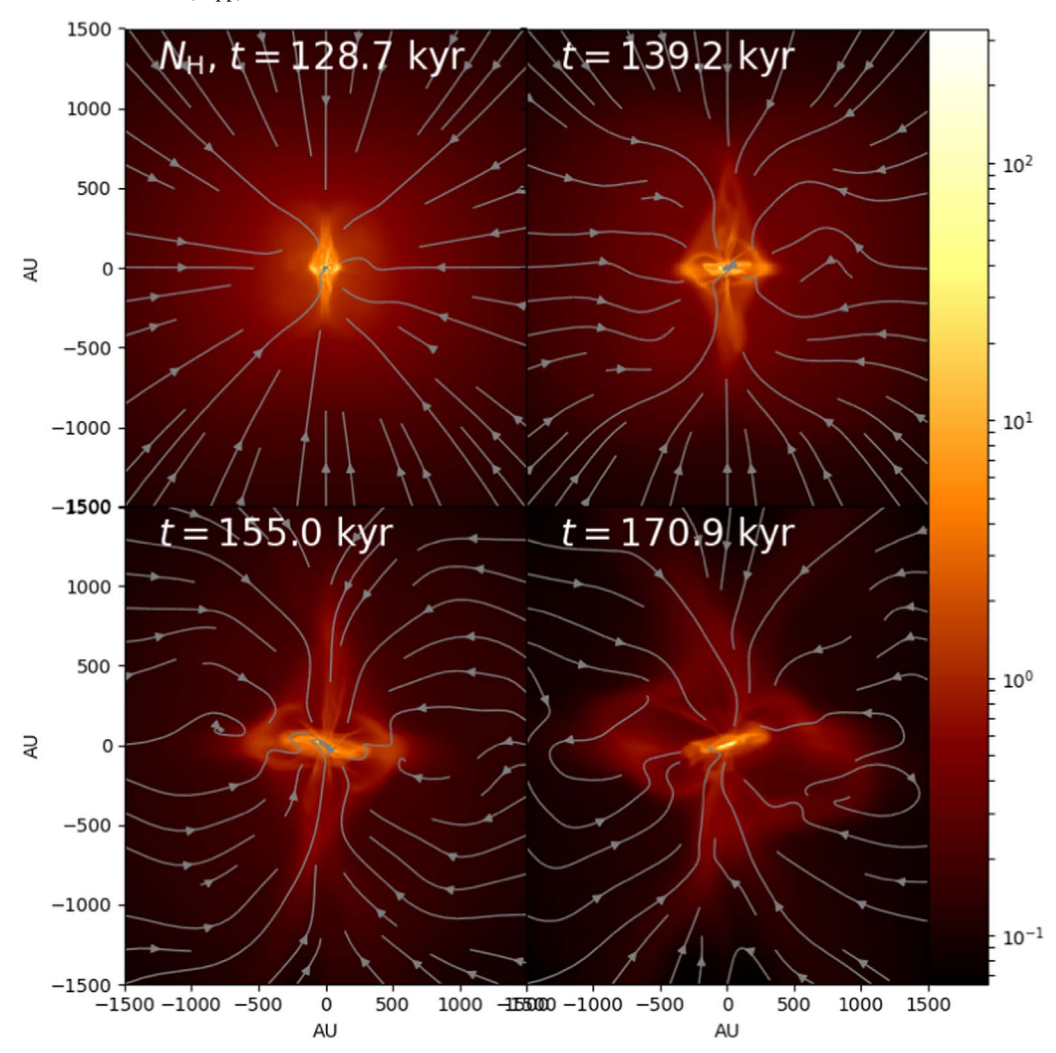


Figure 8. Time development of the *infunnel* of model H in large scale. The colors refer to column densities. The infunnel, an axial funnel-shaped infall stream, can be perceived as the cone-like enhanced column density extending in the vertical direction.

5. Discussion

We have categorized the numerical results of LKS13 into four types based on 3D time evolution with PERSPECTIVE. While we give consideration to all of them for their own right, it is apparent that only CS and LS models show signs of disk formation and therefore will be discussed in more detail for their observable features. While individual dynamical evolution carries a strong dependence on the initial conditions, the polarization effect alone may not secure a conclusive distinction. Velocity profiles with deviations from circular Keplerian velocities can tell us about the effects of magnetic braking done to the systems. Recent results from Class 0 objects VLA 1623A and IRAS 16293 can also serve as convenient references for comparisons.

5.1. Hydromagnetic Spiral Inflow

The CS and LS disks and their surroundings are systems of magnetically confined flows. The general pattern of rotational inflow (see Section 4.6 and Figure 18) flows inward in a curved trajectory with two arms directed by the analogously structured magnetic field. This phenomenon is known as the pseudo-disk, which LKS13 described as a "snail shell" shape, also denoting

the pseudo-disk as "pseudo-spirals." Coined by Galli & Shu (1993), a pseudo-disk is a disk-like inflow structure that results from magnetic inflow following pinched field lines of the collapse. A pseudo-disk superficially resembles the disk, but it is not fully rotationally supported. Rather, its motions are dominantly supersonic inflows, typically slowed down from freefall speeds by a combination of rotation and magnetic tension forces. However, the general direction of the field lines in our CS and LS cases is orthogonal to the Galli & Shu (1993) scenario, perhaps pronouncedly so, as Galli & Shu (1993), being pioneering work, did not include (misaligned) rotation.

In the case of CS, the rotating vertical inflow is strongly streaming toward the pseudo-spiral ridges already at $R \sim 1000\,\mathrm{au}$. In the LS, the effect is there, but it is more chaotic. These would demonstrate that the magnetic forces are directing the collapse dynamics in the manner of a pseudo-disk, after the initial magnetic field has sufficiently condensed. This could be the reason why the approximate disk height is determined already early on in the development (Figure 14), with the magnetic field directing the system into such a configuration. A noteworthy feature is that when the inflow streams along the pseudo-spirals that connect to the spiraling inner disk, there is no clear presence of a centrifugal shock. The

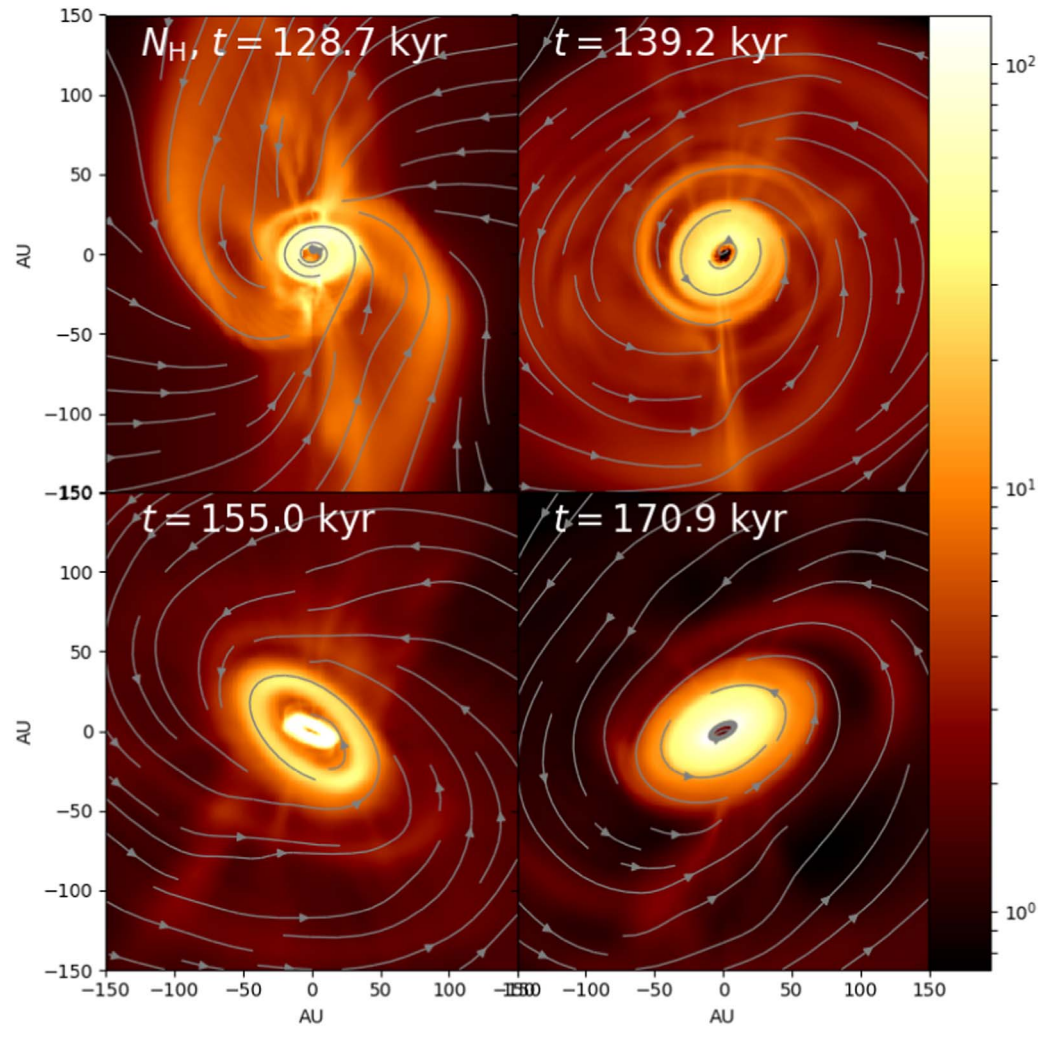


Figure 9. Precession of the disk in model H seen in small scale at a 45° angle. The colors refer to column densities.

transition between disk and pseudo-disk is smooth, in contrast to the more standard pseudo-disk scenario with aligned rotation and magnetic fields (Krasnopolsky & Königl 2002).

In both CS and LS cases there is a trailing spiral inflow of matter that is visible in the column densities (Figures 1, 2, 4, 5, and 9), leading from the lobes of pseudo-spirals toward the inner disk, which is potentially observable. LKS13 argue that the spiral is strongly influenced by magnetic torques, and the spiral inflow is an essential part of the collapse process, as this is how inflow is most efficient. Indeed, similar pseudo-disk behavior is even present in the LA case, where there is a (less bent) pseudo-spiral but no disk. However, as the system extends from the inner spirals of the disk to the infall lobes of the pseudo-spirals, they become increasingly difficult to observe, due to the lack of density and therefore emission. Despite demands on sensitivity, detecting parts of the pseudodisk should be considered a priority for detecting the magnetically misaligned collapse, as it is one of the most distinctive features of the model. While the spiral structures are visible in polarization (see Figures 1, 2, 4, and 5), the effect is weak and can be very difficult to detect, due to the distorting influence of noise (see Figures 11 and 12). Because any rotating disk system can be expected to have wound-up toroidal magnetic field due to rotation, merely observed toroidal field cannot conclude its origin.

Most of the above features will be visible with reasonable inclination, but the features of spirals and pseudo-spirals will become less conclusive when viewed edge-on, with the inner part resembling merely a disk-like object. However, the pseudo-spirals are effectively visible as additional low-density lobes in the midplane, if they are favorably aligned with the LOS. Finding such features around the edge-on disk observation would support the misaligned collapse scenario, although this would require more careful assessment of the object in question.

5.2. Hydromagnetic Precession

The LS-case disk shows precessing motion (see Section 4.2 and Figure 9). The magnetic field is likely the primary cause of this phenomenon, because the weaker-field CS case does not show precessing behavior. LKS13 found with models P and Q that what they called a "porous" disk, or our LS case, would emerge with approximately $\lambda > 4$. Unfortunately, they did not probe the transition from the model G CS case to the model H LS case, and therefore we cannot know at which stage the dynamical precession behavior emerges after the magnetic field strength increases.

A possible explanation for the precession could be found based on the anisotropic nature of the magnetic effects.

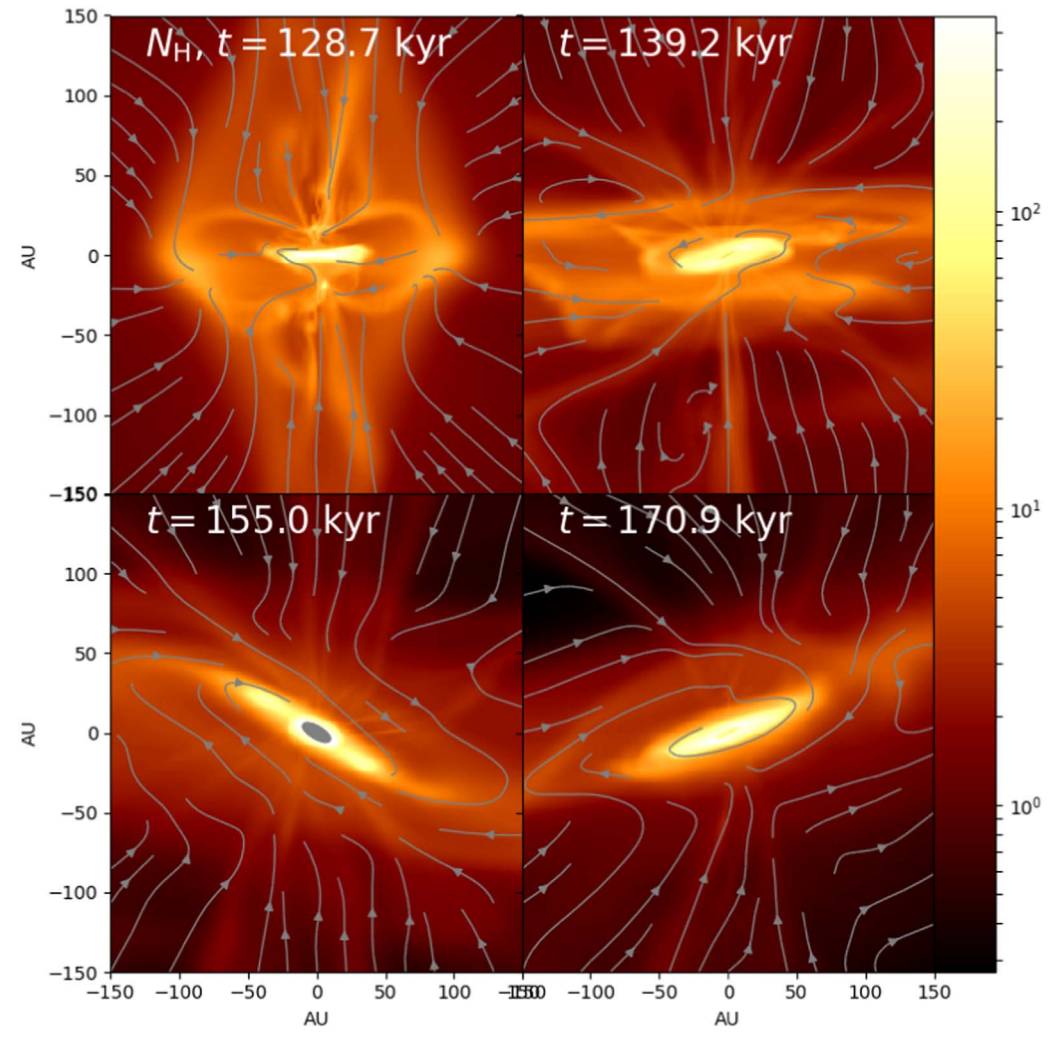


Figure 10. Time development of the infunnel of model H in small scale. The colors refer to column densities.

Consider a case of wound-up magnetic field: from initial collapse, the magnetic field is dragged by the collapsing flow into the typical hourglass geometry and field lines are wrapped up by the rotation. Over time, this magnetic tension tries to relax itself, but because the angular momentum is strong, the energy is released into the vertical motions, leading to precession-type oscillation. However, investigating this conclusively is beyond the scope of this study.

5.3. Axial Infall Streams and Outflows: The Infunnel

In Section 4.1 we observed that some matter flows in through the polar directions like a magnetic funnel-shaped infall stream (for short, an *axial infunnel*), along which the infall material spirals toward the central object itself (see Figures 8–10). The infunnel can lead to some confusion, if the flows themselves are not properly examined. Particularly, the shape of the infunnel in LS can resemble an outflow cavity. If only the gradient of velocity is seen, without another kind of supporting evidence for an outflow, inflow could be mistaken for an outflow. This could be a point of concern when tracing outflow structures in smaller scales (e.g., Bjerkeli et al. 2016), where observations are at the limits of instrument sensitivity. Even when observed in movement without proper velocity information, the edges of the infunnel appear seemingly like

that of an outflow, because there are wave motions moving outward from the center. However, the direction of these waves is opposite to their flow direction.

Outflows in the LS case, on the other hand, only appear as bullet-like, sporadic pulses of ejected matter, which follow the inclination of the disk. A potential mechanism for the phenomenon could the magnetic tower jet (Lynden-Bell 2003; Kato 2007), as it is primarily dependent on the wrapping of the toroidal magnetic field. The mechanism could lead to the release of angular momentum after sufficient magnetic energy has gathered. LKS13 do not make note of the outflow in model H, but it is clearly visible from the time development of velocities and columns density. However, we cannot know how the outflow would behave over a long period of time.

5.4. Patterns of Rotation

Another supportive signal for misaligned collapse would be found if some rotational velocities of the disk could be estimated. The wave-like perturbations from a velocity profile with a Keplerian power-law index with respect to the central mass, depicted in Figures 17 and 18, could provide such signatures. Such deviations from circular Keplerian velocities will appear despite the accurate assessment of the central mass. However, a fit to the velocities with a Keplerian power law

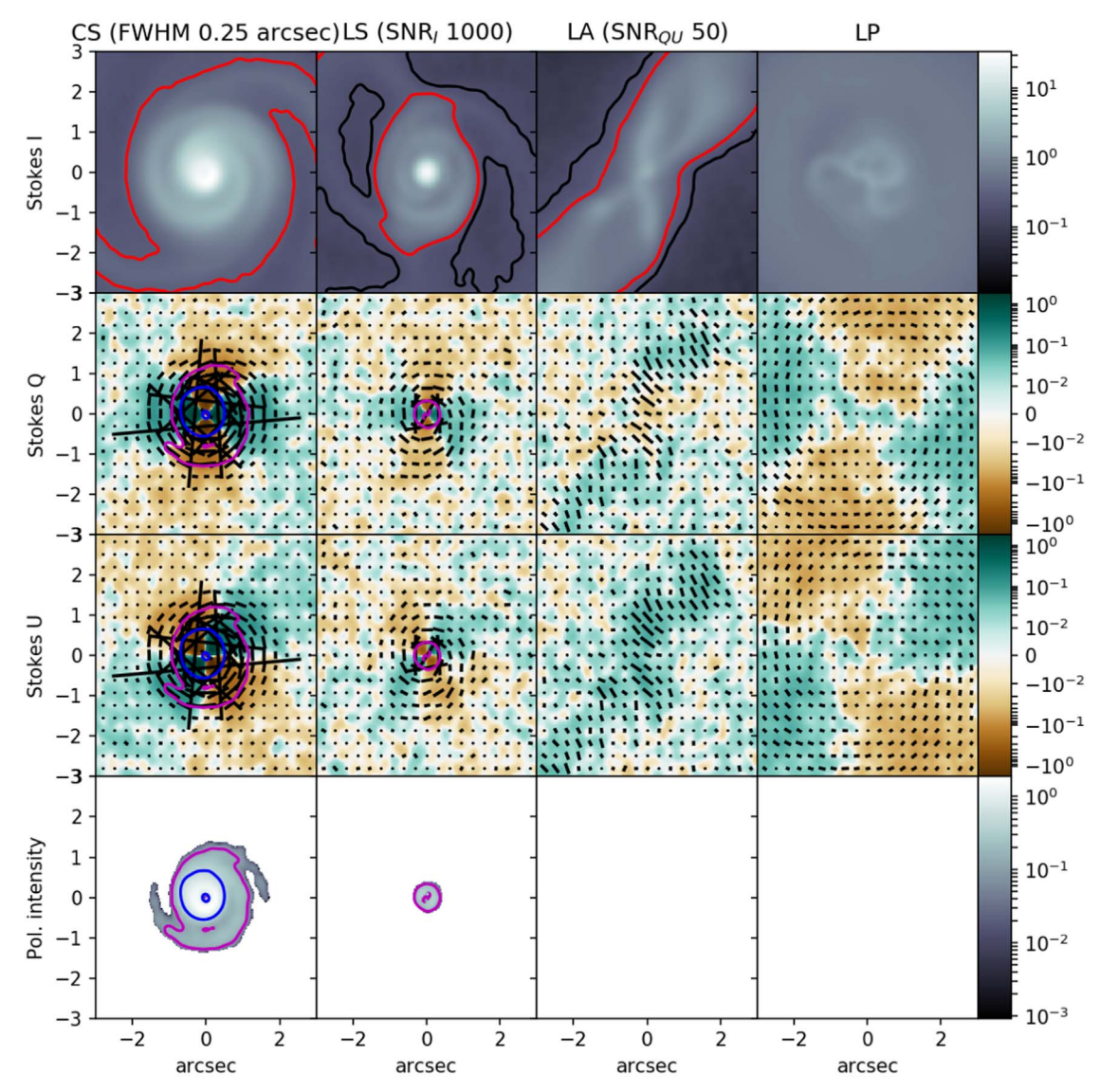


Figure 11. Models G, H, I, and A viewed from above, with 0.25 arcsec FWHM and S/N \sim 1000 and \sim 50 for Stokes I and Q/U, respectively. The red contour shows the regions with 5σ detection, and the black contour that with 3σ . The magenta and blue contours show where $\mathcal{P}_I/\sigma_{PI} \geqslant 1$ and 4, respectively.

faces a number of challenges if the intent is to understand the kinematics of an observed object. In addition to the issues raised here, Harsono et al. (2015) have performed CO line modeling based on a part of the LKS13 data set (models A and G), giving some sense of observing the velocities in practice.

Our PV diagrams demonstrate one of the concerns. Most of the radial velocities are seen below the Keplerian power law predicted by the mass of the central object, which in our case is well known. Physically this is reasonable: magnetic torques slow down rotation (LKS13), and there is substantial inflow toward the center. However, if a Keplerian power-law fit is done to an observed PV distribution, where M_* is not known, M_* could be underestimated, because the disk is consistently sub-Keplerian on average as shown in Figure 19, with occasional components being super-Keplerian with respect to the central mass. We also know that the rotation in the disk is influenced not only by the central object mass but also by self-gravity of the disk. Therefore, development of kinematic spiral flow models, for PV diagram fitting, could prove to be useful.

Our spiral flows also demonstrate that the circular Keplerian velocity assumption can be simplistic. The nature of the spirals

in our collapse scenario is likely hydromagnetic, as described in Section 5.1. Formation of spirals in a disk is in principle possible with purely hydrodynamical accretion streams during collapse (Hennebelle et al. 2017). Due to an increase in kinetic energy, the inner disk is not likely directed merely by magnetic forces, but as LKS13 point out, the snail-shell-shaped pseudodisk significantly directs the inflow of the collapse, making it at least partially responsible for the shape. In addition, a stronger magnetic field can inhibit rotation, as is seen in the LS case. Therefore, the system as it is would not be the same without the magnetic fields. The pseudo-spirals surrounding the system present a corresponding type of velocity perturbations as the spirals in the rotational supported disk, with dense parts approaching the circular Keplerian/super-Keplerian velocities with respect to central mass and low column density areas appearing sub-Keplerian in the CS case.

The apparent variation of rotational velocities (between above and below the circular Keplerian speed $v_{\rm kep}$) in the rotationally supported part of the disk can be best understood with eccentricity. The disk is approximately Keplerian with a component of accretion, but this rotation is not circular.

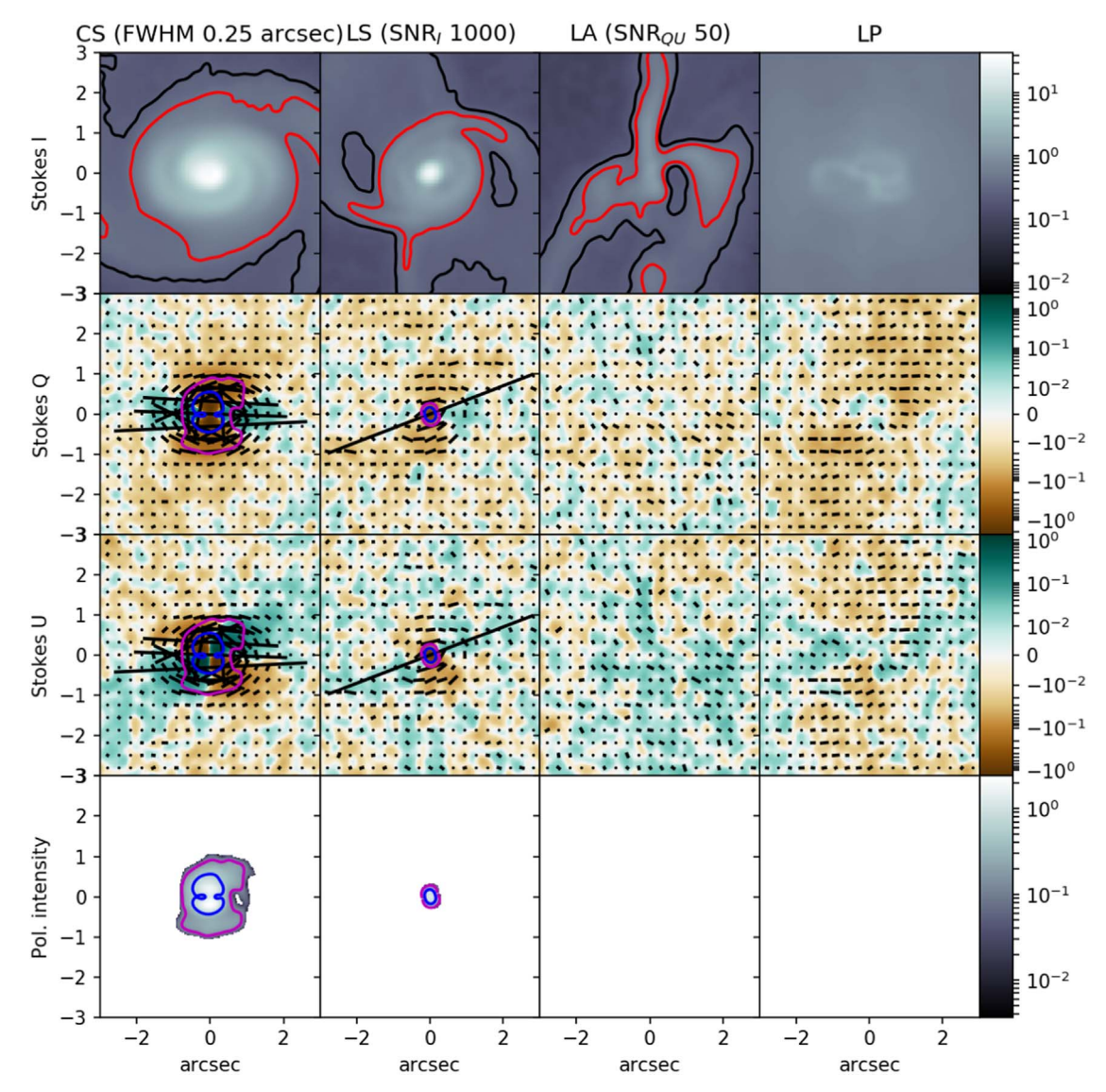


Figure 12. Models G, H, I and A viewed from a 45° inclination, with 0.25 arcsec FWHM and S/N \sim 1000 and \sim 50 for Stokes I and Q/U, respectively.

Instead, the velocity flows follow eccentric orbits. When the eccentric orbits approach periastron, the fastest rotation velocities can be found, slowing down near apastron. They also correspond well with positive and negative radial velocities with respect to the center. Therefore, a significant part of the deviations are due to the fact that while rotation approaches the circular Keplerian velocities as defined in Equation (9), the rotation is not circular.

5.5. Planets?

Spirals can be formed also by other processes than the magnetic collapse. Our velocity analysis was inspired by the methods used in studies of spiral structures that can emerge owing to the influence of giant planet formation in the disk due to a pressure gradient (Kanagawa et al. 2015; Pérez et al. 2018; Teague et al. 2018). Using an equivalent definition of $\delta v_{\rm rot}$ as in Teague et al. (2018) and Pérez et al. (2018), we can attempt to compare how the magnetically driven spirals differ from planet-driven ones. However, it should be emphasized that the disks in our MHD models are of significantly earlier stage than even the youngest objects where planet formation is currently

concerned, such as HL Tau (Testi et al. 2015). What this comparison does is give an intuitive comparison to the magnitude of our spiral phenomenon.

Teague et al. (2018) based their estimate on matching observed velocity profiles with a hydrodynamical disk model. Their model of two Jupiter-mass planets generates deviations from the circular Keplerian velocity, $\delta v_{\rm rot}$, between \sim -6% and \sim 3%. On the other hand, Pérez et al. (2018) model their synthetic observations with planets as massive as $10\,M_{\rm Jupiter}$, generating $\sim\pm20\%$ velocity perturbations in $\delta v_{\rm rot}$. While the perturbations in Teague et al. (2018) are relatively weak, the hydromagnetic spirals of our model can appear as perturbations of roughly equivalent magnitudes compared to the Pérez et al. (2018) model, especially in the inner disk (see Figure 18). We cannot know, however, how well our velocity perturbations will last further as the disk develops to a stage where planet formation is possible.

5.6. Comparison to Observations

We have considered VLA 1623A (Murillo et al. 2013; Harris et al. 2018; Sadavoy et al. 2018a) and IRAS 16293

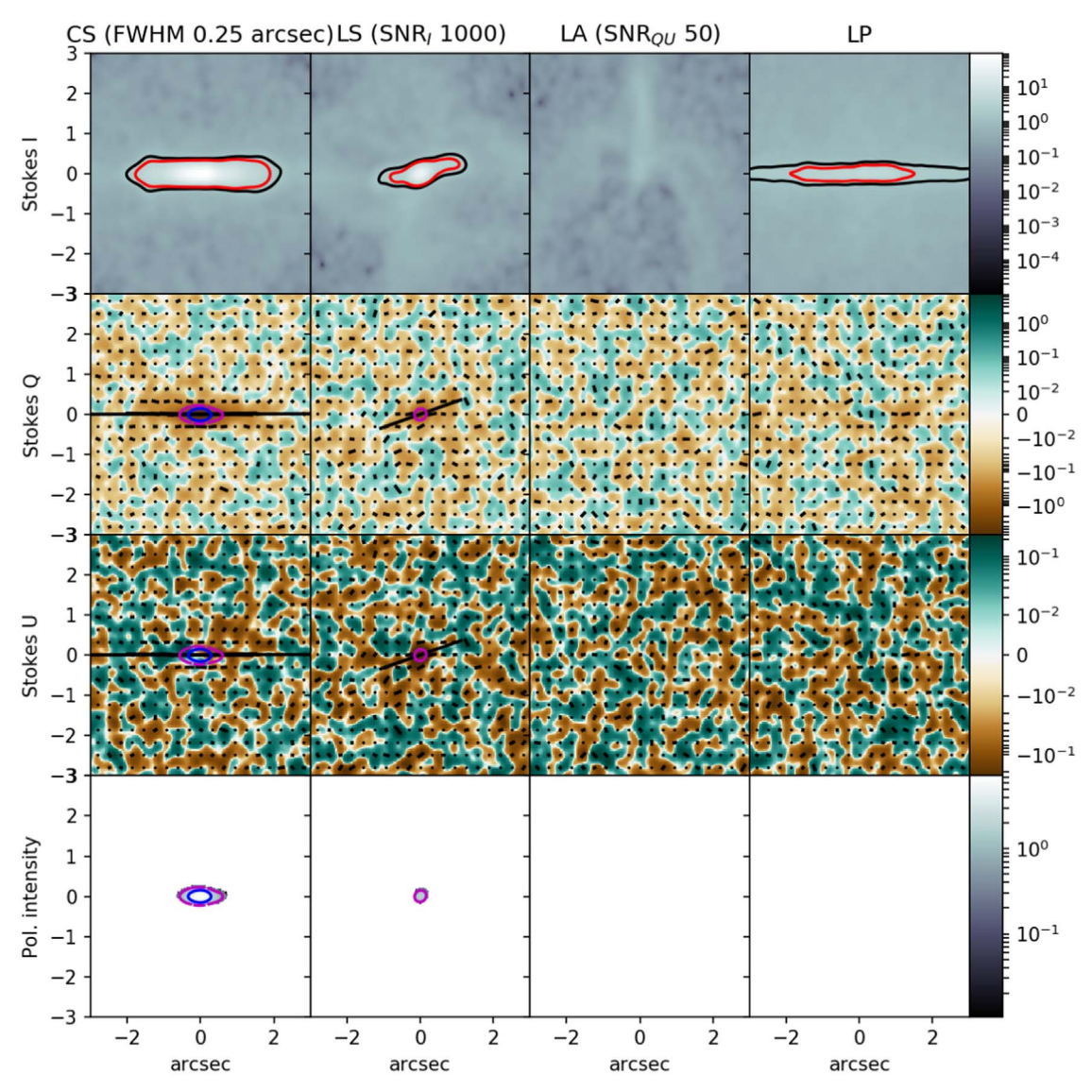


Figure 13. Models G, H, I, and A viewed from a 45° inclination edge-on, with 0.25 arcsec FWHM and S/N ~ 1000 and ~ 50 for Stokes I and Q/U, respectively.

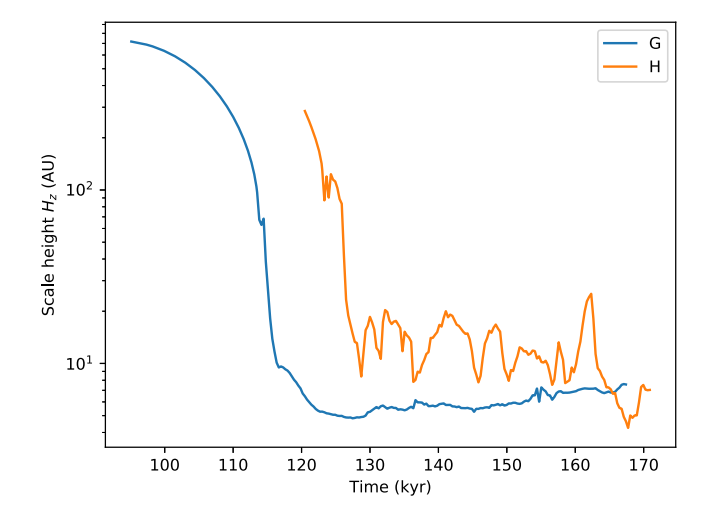
(Sadavoy et al. 2018b) as potential candidates for misaligned formation. As more high-resolution observations of Class 0 objects are published, perhaps more potential candidates can emerge, but these two can function as examples of current possibilities and limitations.

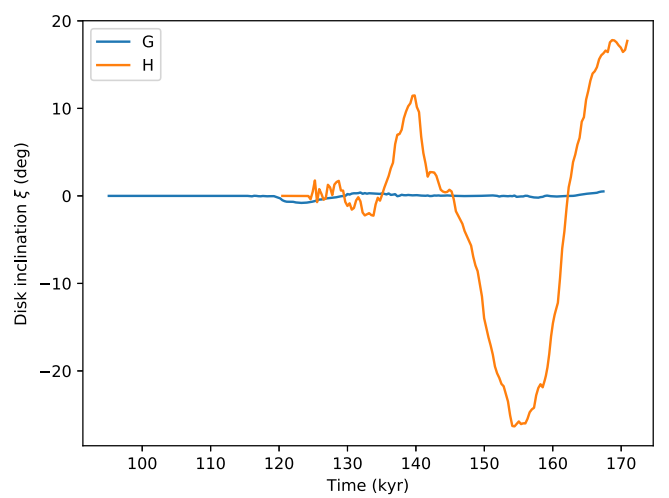
Sadavoy et al. (2018a) observed VLA 1623A in ALMA Band 6 (1.3 mm) continuum with Stokes I, Q, and U. In addition to the brighter central disk, they saw ring-like pseudodisk surroundings around VLA 1623A. This surrounding extended envelope shows a spiraling structure in the pseudodisk, reminiscent of the spiraling inflows discussed in our study, making VLA 1623A a potential candidate. Harris et al. (2018) repeated a similar observation but with polarized $872 \,\mu\text{m}$ dust emission. They discovered that VLA 1623A contained two inner components and that their polarization matched well the 1.3 mm observations. The polarization directions along the ring of Sadavoy et al. (2018a) follow a different pattern from ours, although Harris et al. (2018) deduce that observed polarization is likely a result of self-scattering and not of magnetic alignment. Therefore, polarization estimates are inconclusive in terms of our model. Observations

focused on the VLA 1623A ring/pseudo-disk could illuminate the matter further.

For VLA 1623A, Murillo & Lai (2013) show that there is an outflow, with potentially two components, emerging from the object. While our LS case produces an outflow, it is not continuous, which is in conflict with the observation. However, LKS13 did not focus on modeling the outflow development. Model H shows tentative hints that a more continuous, narrow outflow could be happening, but the data set is too short to be conclusive. Therefore, extending the simulation beyond the current end point might address whether a more stable outflow would emerge at a later stage. In both model G and model H, the velocity of the polar inflow is ~0.4 km s⁻¹ in magnitude, which is supersonic, but slower than, e.g., Bjerkeli et al. (2016; 2.5–5.5 km s⁻¹) TMC-1A or Murillo & Lai (2013; 2–15 km s⁻¹) VLA 1623 outflows. This is approximately half of the freefall velocity with respect to the central point mass.

Looking at VLA 1623A, Murillo et al. (2013) measured radial velocities from $C^{18}O$ line emission. Their radial velocity measurements did not show direct spiral signatures; they found that their infall + Keplerian rotation model fit best to their





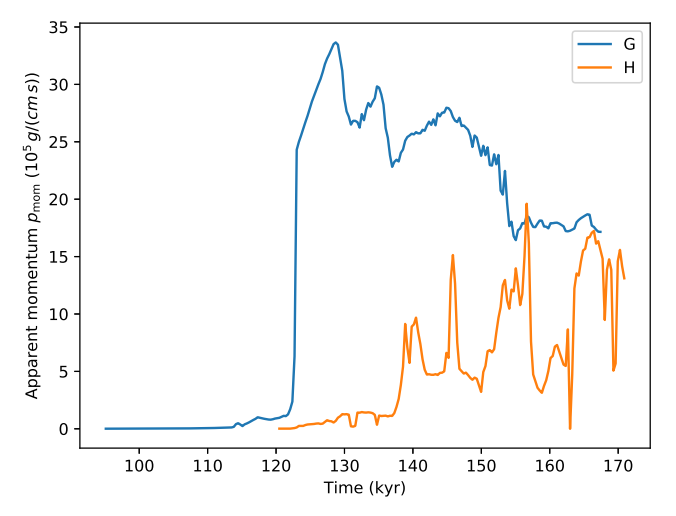


Figure 14. Evolution of scale height H_z (top), precession angle ξ (middle), and apparent momentum p_{mom} (bottom) as a function of time.

observed PV distribution, which is at least coherent with the picture presented in our study. Because of the observational challenges regarding polarization, more light could be shed on the surrounding ring by carefully examining velocities of the VLA 1623A pseudo-disk, as our model would suggest

spiraling variations in the velocity field. In such a way, observing the velocities of VLA 1623A could also tell us something about its magnetic nature.

In light of our results, the observations of IRAS 16293 by Sadavoy et al. (2018b) are also intriguing (see also Rao et al. 2009; Liu et al. 2018, for other polarization measurements). They performed their observations in ALMA Band 6 (1.3 mm) continuum with Stokes I, Q, and U, essentially following a comparable approach to Sadavoy et al. (2018a). However, using two separate pointings, they got a measurement of a part of the extended emission between the IRAS 16293 A and B components. There they find polarization structures, which they call "Streamers" and a "Bridge."

The IRAS 16293 system is clearly more complicated than our spherically symmetric model. However, if we can believe that the polarization vectors around the edges of the IRAS 16293B disk trace magnetic fields, we have a case of magnetic alignment similar to what we see as spiraling inflow—where the magnetic field is bending in a rotational direction around toward the central disk. Therefore, there would be magnetic field lines that outside of the disk align with rotational inflow analogous to our pseudo-disk spirals. In such a case, the Bridge and B-Streamer of Sadavoy et al. (2018b) are good candidates for pseudo-spiral-type inflow.

6. Conclusions

We have examined the time development of the MHD models of LKS13 using our radiative transfer code PERSPEC-TIVE. The MHD models were created to test the effects of misaligned (especially orthogonal) rotation axis and magnetic field direction during prestellar core collapse to solve the magnetic braking catastrophe. LKS13 found that misalignment could make disk formation possible if the mass-to-flux ratio was $\lambda \gtrsim 4$. We have used PERSPECTIVE to continue the earlier analysis by showing how the examined systems would be visible in terms of column densities and Stokes I, Q, and U. We also analyzed how the velocity profile behaves in relation to what was seen and how the disk differs from a simple circular Keplerian orbit. The 3D view of the simulation results and their time evolution has offered a number of insights not well visible from the more traditional cut-slice approach. In a collapse model not all features are aligned with well-determined planes or reach a genuine steady state. Therefore, those features will be missed by a slice cut or by a single snapshot of the intrinsically 3D and time-evolving system.

We prepared a face-on view movie of CS model G, showing column density together with streamlines. From that movie we learn that the gas makes strongly eccentric and approximately elliptical orbits during its infall. These infalling elliptical orbits constitute an inspiraling motion. The inner and outer turning points of that motion (roughly the periastron and apastron of the orbits) correspond to regions of increased column density; these dense regions largely match the ridges of (respectively) the inner and outer parts of the disk spirals as seen in the column density view. These eccentric orbits are not exactly Keplerian; we know that kinematically because of their visible infall, and we know that dynamically owing to the presence of a substantial self-gravity. Self-gravity is presumably the cause of the observed precession of the periastron (by making the orbits not closed), and visualizations show that it can exert

torques. Magnetic forces are also known to be present in this system. Further study of this matter may require new simulations, including (1) tracer fields helping to follow streaklines in addition to streamlines, and (2) alleviating the disruptive effects of the numerical inner boundary conditions to the inner spiral when the periastron of the eccentric orbits becomes comparable to 6.7 au. For now we are ready to state that in addition to the disk spirals visualized and possibly detectable as a column density, the spirals visualized as streamlines allow us to say that the channel of motion is not necessarily exactly equal to the location of the spiral ridge path of highest densities, due to the presence of these eccentric orbital motions.

With these methods we improve our understanding of the MHD model and of its observable properties. In terms of the physical model we see the following:

- Collapse of a prestellar core with magnetic field perpendicular to the rotation axis leads to a spiral-like system. Formation of the disk is affected by a snail-shellshaped pseudo-disk, having the projected appearance of a spiral.
- 2. The system is in the state of constant change and movement. Many of its essential features do not become visible without looking at their time evolution.
- 3. Magnetic forces that can lead to visible precession of the disk during formation.
- 4. Funnel-shaped axial infall flow (*infunnel*) along polar directions is present during misaligned collapse.
- 5. There is no visible continuous outflow at this early stage of misaligned collapse. If it happens, it is momentary and bullet-like.
- 6. Spirals appear as velocity variations from circular Keplerian orbital velocity. Generally velocities are sub-Keplerian, especially in the LS case, but in the CS case super-Keplerian motions are possible in the inner disk along the spiral ridges. Some of the super-Keplerian effects are present owing to eccentricity of disk rotation.

We found a number of potentially observable features connected to misaligned disk formation. The following features could provide a reasonable indicator of misaligned collapse:

- 1. The general shapes of the RSDs are distinctively spiral-like, particularly with spiral-like pseudo-disk in surroundings.
- 2. Magnetically aligned dust polarization is dominated by the azimuthal direction of the magnetic field. Spiral characteristics can be found at the boundary of the disk and pseudo-disk. However, the actual spiral characteristics can be lost, with noise affecting polarization. Therefore, high sensitivity is required.
- 3. Observing spiral-like perturbations from velocity profiles with a Keplerian power-law index could be the best way of recognizing the magnetic spirals. These perturbations should extend to the pseudo-disk.
- 4. The infunnels that appear during the collapse process could easily be mistaken for an outflow cavity if viewed sideways. However, as low-density areas they might be too faint to be visible.

With improved modeling efforts and as new results emerge from ALMA of early prestellar objects, the misaligned disk model could be further tested. Misalignment of rotation axis and magnetic field presents one aspect of disk formation, separate from pure turbulent reconnection diffusion or non-ideal MHD effects. While the reality will likely be some combination of all of them, recognizing the type of influence of all such processes will help us to understand what is most important in which stage and context.

The authors thank Prof. Ronald Taam for useful conversations during the research process. Z.Y.L. is supported in part by NSF grants AST-1815784 and AST-1716259 and NASA grants 80NSSC18K1095 and NNX14AB38G. K.H.L. acknowledges support from an NRAO ALMA SOS award. This work utilized tools developed by the CHARMS group and the computing resources and cluster in TIARA at Academia Sinica. This research has made use of the SAO/NASA Astrophysics Data System.

Appendix Velocity Averages and Gaussian Fitting

A.1. Velocity Averages

To see how the observed maps relate to apparent velocities in the system, we calculate the LOS velocity averages for all Cartesian components v_{LOS} , v_{W} , and v_{N} —or LOS, west, and north directional velocities, respectively—as a density-weighted average:

$$\langle v_k \rangle = \frac{1}{\Sigma} \int \rho v_k \, ds. \tag{11}$$

Here k denotes any velocity component. While only v_{LOS} would be observable in principle, all components can help with understanding the results in physical terms.

In this study, when streamlines are plotted or radial, poloidal, and toroidal velocity components are discussed, they are calculated from the Cartesian velocity averages, assuming counterclockwise rotation of the system. Therefore, they are averages by projection, but not picked up directly from a cut from the 3D model. This approach serves well when relating velocities to the also otherwise projected structures of column densities and Stokes parameters.

A.2. Gaussian Fitting

We approached quantifying the time development with Gaussian fitting. For this, we focused on the edge-on observations (with the disk placed largely along the horizontal direction), as other viewing angles are not well suited for the method, which worked as follows.

First, we fitted a Gaussian profile to the Stokes I maps along the vertical direction for all horizontal points. This allowed us to get the local maximum intensity $I_{\max,i}$, distribution center Z_i , and width of the disk $H_{z,i}$, as in

$$I_i(z) = I_{\max,i} \exp\left(-\frac{(z - Z_i)^2}{H_{z,i}^2}\right),$$
 (12)

where i is a pixel column along the horizontal axis.

Based on the fit, we tried to estimate a number of disk properties and how they change by taking further averages. There are essentially the scale height H_z , disk tilt angle ξ , and peak locations ζ_E and ζ_W .

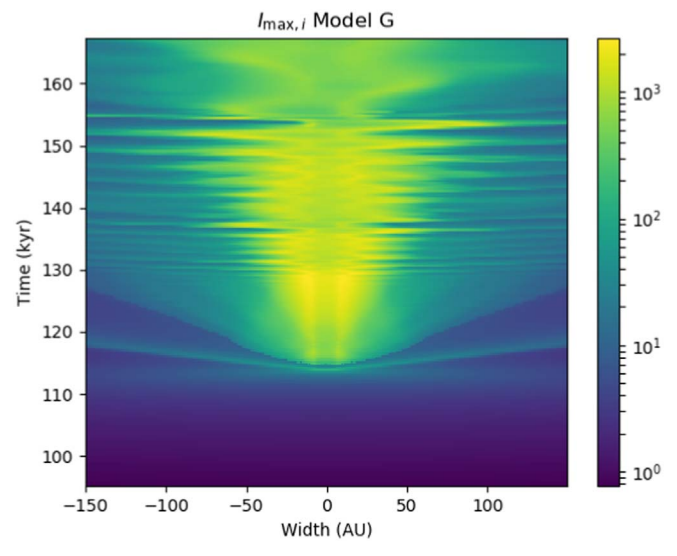
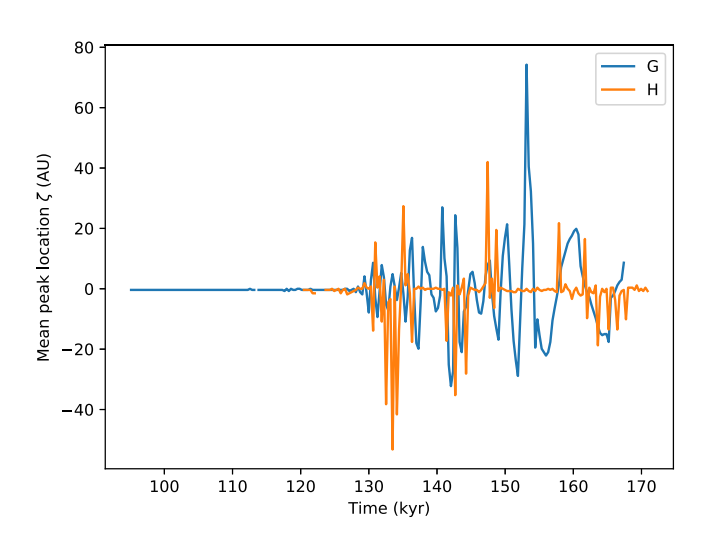


Figure 15. $I_{\max,i}$ as a function of time for model G.



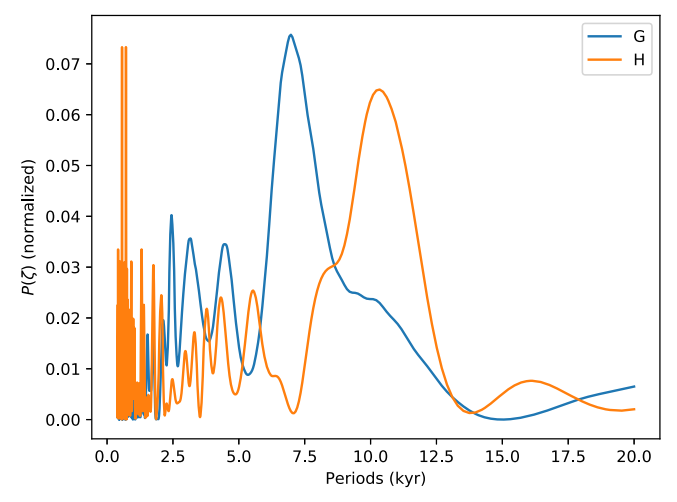
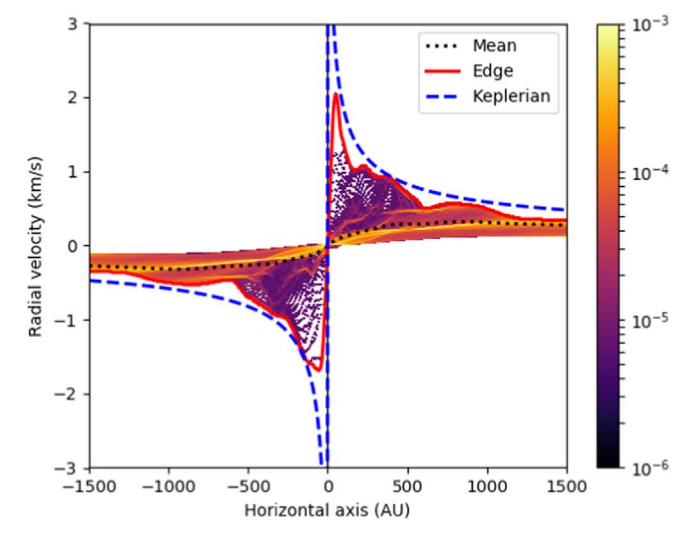


Figure 16. Top: mean peak location ζ as a function of time. Bottom: normalized Lomb–Scargle periodograms $P(\zeta)$, as a function of period T.

The height H_z is calculated simply as an $I_{\max,i}$ weighted average of $H_{z,i}$. The angle ξ is derived by making a linear fit to Z_i and calculating the relative angle of the fit, so that $\xi = 0^{\circ}$



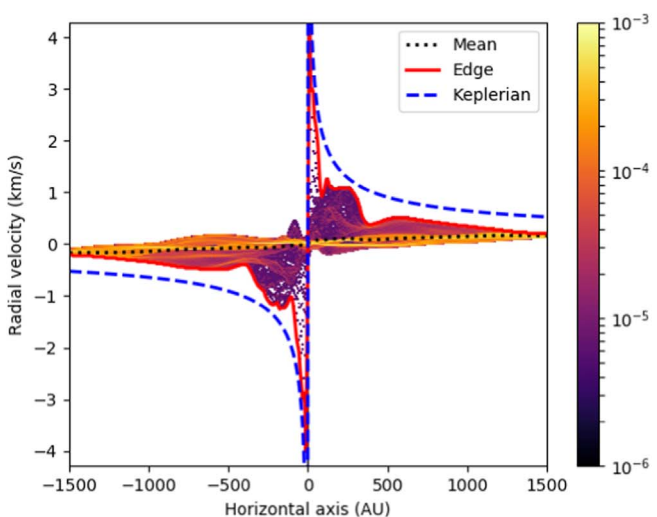


Figure 17. PV diagrams of model G (top) and model H (bottom). The colors represent probability density with the total pixel count. The red line denotes the largest velocities at the given horizontal coordinate, and the hatched line traces $\nu_{\rm kep}$ based on M_* .

denotes the situation where the disk is perfectly horizontal. The average peak location $\zeta = (\zeta_E + \zeta_W)/2$ is used to trace oscillations of the disk plane itself. The visible density of the disk is not horizontally uniform. There are local maxima in the intensities on both sides of the sink particle/inner boundary (see, e.g., Figure 15). Therefore, we trace the locations of such peaks, ζ_E on the east side and ζ_W on the west side, and trace their position over time, after taking an average, resulting in Figure 16 (top panel). Results of the Gaussian fitting analysis are presented in Section 4.5.

Apparent momentum p_{mom} was calculated by taking the average of $\Sigma |\langle v_{\text{LOS}} \rangle|$ around the fit axis, or

$$p_{\text{mom},i} = \langle \Sigma | \langle v_{\text{LOS}} \rangle | \rangle_{Z_i - H_{z,i}/2}^{Z_i + H_{z,i}/2}. \tag{13}$$

While this is not an accurate measurement of the true momentum, it can function as a comparative measure between model results, functioning as a diagnostic variable when tracing the time evolution of motion.

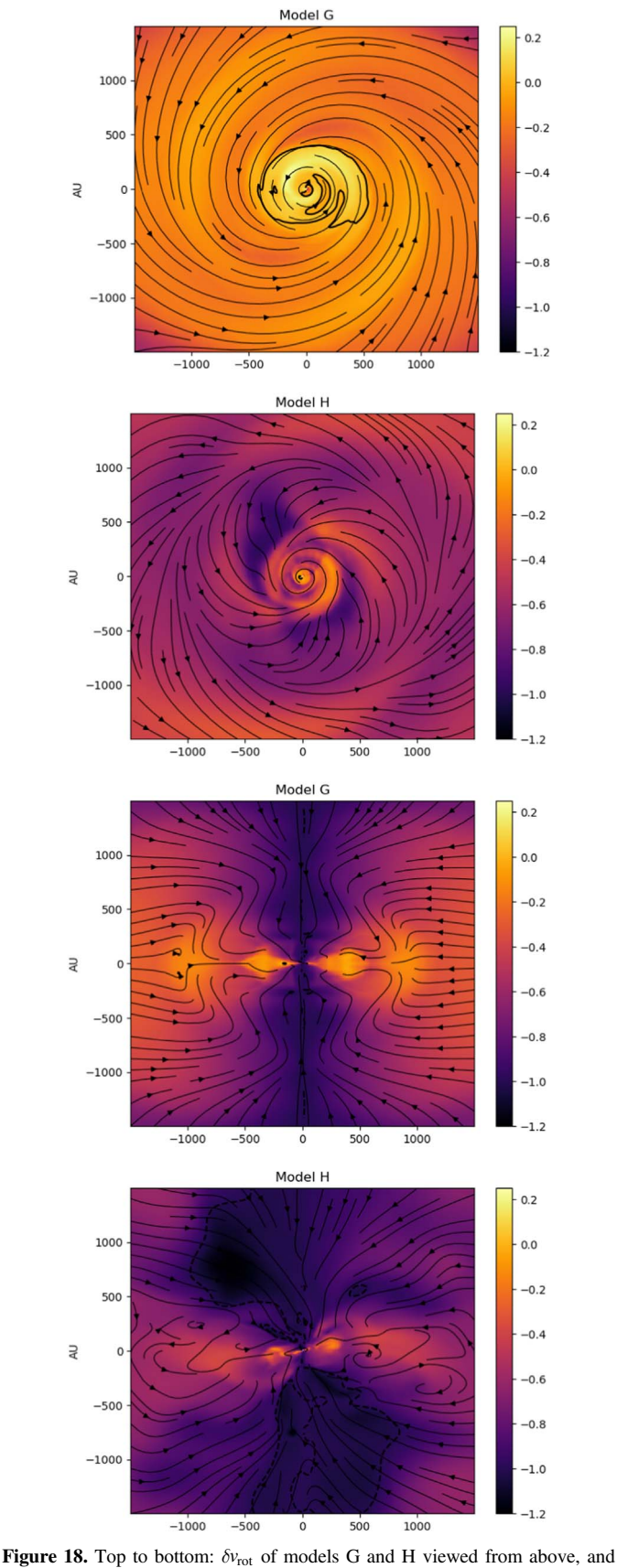


Figure 18. Top to bottom: δv_{rot} of models G and H viewed from above, and δv_{rot} of models G and H viewed edge-on. It should be noted that in the edge-on case v_{kep} is calculated relative to the origin of the horizontal axis instead of the central point.

(An animation of this figure is available.)

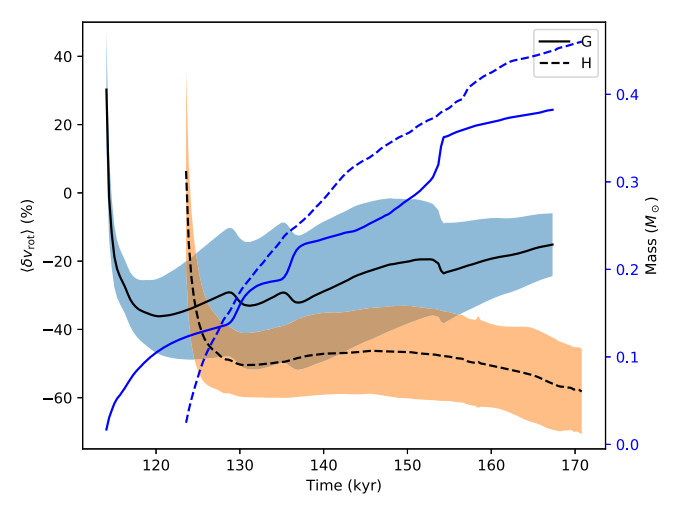


Figure 19. Time development of $\langle \delta v_{\rm rot} \rangle$, starting from the point where $M_* > 0.01 \, M_\odot$. The colored areas show the corresponding range of one standard deviation, $\sigma_{v.{\rm rot}}$.

ORCID iDs

Miikka S. Väisälä https://orcid.org/0000-0002-8782-4664 Hsien Shang https://orcid.org/0000-0001-8385-9838 Ruben Krasnopolsky https://orcid.org/0000-0001-5557-5387

Sheng-Yuan Liu https://orcid.org/0000-0003-4603-7119 Ka Ho Lam https://orcid.org/0000-0003-3581-1834

References

```
Allen, A., Li, Z.-Y., & Shu, F. H. 2003, ApJ, 599, 363
Aso, Y., Ohashi, N., Saigo, K., et al. 2015, ApJ, 812, 27
Bjerkeli, P., van der Wiel, M. H. D., Harsono, D., Ramsey, J. P., &
  Jørgensen, J. K. 2016, Natur, 540, 406
Bodenheimer, P. 1995, ARA&A, 33, 199
Dapp, W. B., & Basu, S. 2010, A&A, 521, L56
Fiege, J. D., & Pudritz, R. E. 2000, ApJ, 544, 830
Galli, D., Lizano, S., Shu, F. H., & Allen, A. 2006, ApJ, 647, 374
Galli, D., & Shu, F. H. 1993, ApJ, 417, 243
Gray, W. J., McKee, C. F., & Klein, R. I. 2018, MNRAS, 473, 2124
Harris, R. J., Cox, E. G., Looney, L. W., et al. 2018, ApJ, 861, 91
Harsono, D., van Dishoeck, E. F., Bruderer, S., Li, Z. Y., & Jørgensen, J. K.
   2015, A&A, 577, A22
Hennebelle, P., & Ciardi, A. 2009, A&A, 506, L29
Hennebelle, P., & Fromang, S. 2008, A&A, 477, 9
Hennebelle, P., Lesur, G., & Fromang, S. 2017, A&A, 599, A86
Joos, M., Hennebelle, P., & Ciardi, A. 2012, A&A, 543, A128
Joos, M., Hennebelle, P., Ciardi, A., & Fromang, S. 2013, A&A, 554, A17
Juvela, M., Demyk, K., Doi, Y., et al. 2015a, A&A, 584, A94
Juvela, M., Malinen, J., Montillaud, J., et al. 2018, A&A, 614, A83
Juvela, M., Ristorcelli, I., Marshall, D. J., et al. 2015b, A&A, 584, A93
Juvela, M., Ristorcelli, I., Montier, L. A., et al. 2010, A&A, 518, L93
Juvela, M., Ristorcelli, I., Pagani, L., et al. 2012, A&A, 541, A12
Juvela, M., Ristorcelli, I., Pelkonen, V. M., et al. 2011, A&A, 527, A111
Kanagawa, K. D., Tanaka, H., Muto, T., Tanigawa, T., & Takeuchi, T. 2015,
   MNRAS, 448, 994
Kataoka, A., Muto, T., Momose, M., et al. 2015, ApJ, 809, 78
Kato, Y. 2007, Ap&SS, 307, 11
Korpi, M. J., Brandenburg, A., Shukurov, A., Tuominen, I., & Nordlund, Å.
   1999, ApJL, 514, L99
Krasnopolsky, R., & Königl, A. 2002, ApJ, 580, 987
Krasnopolsky, R., Li, Z.-Y., & Shang, H. 2010, ApJ, 716, 1541
Krasnopolsky, R., Li, Z.-Y., & Shang, H. 2011, ApJ, 733, 54
Krasnopolsky, R., Li, Z.-Y., Shang, H., & Zhao, B. 2012, ApJ, 757, 77
Kuffmeier, M., Haugbølle, T., & Nordlund, Å. 2017, ApJ, 846, 7
Lazarian, A., & Vishniac, E. T. 1999, ApJ, 517, 700
Lee, C.-F., Ho, P. T. P., Li, Z.-Y., et al. 2017a, NatAs, 1, 0152
Lee, C.-F., Li, Z.-Y., Ching, T.-C., Lai, S.-P., & Yang, H. 2018, ApJ, 854, 56
```

```
Lee, C.-F., Li, Z.-Y., Ho, P. T. P., et al. 2017b, SciA, 3, e1602935
Li, Z. Y., Banerjee, R., Pudritz, R. E., et al. 2014a, in Protostars and Planets VI,
   ed. H. Beuther et al. (Tucson, AZ: Univ. Arizona Press), 173
Li, Z.-Y., Krasnopolsky, R., & Shang, H. 2011, ApJ, 738, 180
Li, Z.-Y., Krasnopolsky, R., & Shang, H. 2013, ApJ, 774, 82
Li, Z.-Y., Krasnopolsky, R., Shang, H., & Zhao, B. 2014b, ApJ, 793, 130
Li, Z.-Y., & McKee, C. F. 1996, ApJ, 464, 373
Li, Z.-Y., & Shu, F. H. 1996, ApJ, 472, 211
Liu, H. B., Hasegawa, Y., Ching, T.-C., et al. 2018, A&A, 617, A3
Lizano, S., & Galli, D. 2015, in Magnetic Fields in Diffuse Media, ed. A. Lazarian,
   E. M. de Gouveia Dal Pino, & C. Melioli (Berlin: Springer), 459
Lomb, N. R. 1976, Ap&SS, 39, 447
Lynden-Bell, D. 2003, MNRAS, 341, 1360
Machida, M. N., Inutsuka, S.-i., & Matsumoto, T. 2014, MNRAS, 438,
Machida, M. N., Matsumoto, T., Hanawa, T., & Tomisaka, K. 2006, ApJ,
  645, 1227
Matsumoto, T., Machida, M. N., & Inutsuka, S.-i. 2017, ApJ, 839, 69
Maury, A. J., Girart, J. M., Zhang, Q., et al. 2018, MNRAS, 477, 2760
Mellon, R. R., & Li, Z.-Y. 2008, ApJ, 681, 1356
Mellon, R. R., & Li, Z.-Y. 2009, ApJ, 698, 922
Montillaud, J., Juvela, M., Rivera-Ingraham, A., et al. 2015, A&A, 584, A92
Murillo, N. M., & Lai, S.-P. 2013, ApJL, 764, L15
Murillo, N. M., Lai, S.-P., Bruderer, S., Harsono, D., & van Dishoeck, E. F.
  2013, A&A, 560, A103
Pérez, S., Casassus, S., & Benítez-Llambay, P. 2018, MNRAS, 480, L12
Planck Collaboration, Ade, P. A. R., Aghanim, N., et al. 2015a, A&A,
   576, A104
Planck Collaboration, Ade, P. A. R., Aghanim, N., et al. 2015b, A&A, 576, A105
Planck Collaboration, Ade, P. A. R., Aghanim, N., et al. 2016a, A&A,
```

586, A136

```
Planck Collaboration, Ade, P. A. R., Aghanim, N., et al. 2016b, A&A, 586, A138
Planck Collaboration, Ade, P. A. R., Aghanim, N., et al. 2016c, A&A,
  594, A28
Rao, R., Girart, J. M., Marrone, D. P., Lai, S.-P., & Schnee, S. 2009, ApJ,
  707, 921
Rivera-Ingraham, A., Ristorcelli, I., Juvela, M., et al. 2016, A&A, 591, A90
Rivera-Ingraham, A., Ristorcelli, I., Juvela, M., et al. 2017, A&A,
Sadavoy, S. I., Myers, P. C., Stephens, I. W., et al. 2018a, ApJ, 859, 165
Sadavoy, S. I., Myers, P. C., Stephens, I. W., et al. 2018b, ApJ, 869, 115
Sakai, N., Oya, Y., López-Sepulcre, A., et al. 2016, ApJL, 820, L34
Santos-Lima, R., de Gouveia Dal Pino, E. M., & Lazarian, A. 2012, ApJ,
Scargle, J. D. 1982, ApJ, 263, 835
Simmons, J. F. L., & Stewart, B. G. 1985, A&A, 142, 100
Tazaki, R., Lazarian, A., & Nomura, H. 2017, ApJ, 839, 56
Teague, R., Bae, J., Bergin, E. A., Birnstiel, T., & Foreman-Mackey, D. 2018,
      JL, 860, L12
Testi, L., Skemer, A., Henning, T., et al. 2015, ApJL, 812, L38
Tobin, J. J., Kratter, K. M., Persson, M. V., et al. 2016, Natur, 538, 483
Tomisaka, K. 2002, ApJ, 575, 306
Tsukamoto, Y., Okuzumi, S., Iwasaki, K., Machida, M. N., & Inutsuka, S.-i.
  2017, PASJ, 69, 95
Vaillancourt, J. E. 2006, PASP, 118, 1340
Väisälä, M. S., Gent, F. A., Juvela, M., & Käpylä, M. J. 2018, A&A,
   614, A101
Williams, J. P., & Cieza, L. A. 2011, ARA&A, 49, 67
Yang, H., Li, Z.-Y., Looney, L., & Stephens, I. 2016, MNRAS, 456, 2794
Yen, H.-W., Zhao, B., Koch, P. M., et al. 2018, A&A, 615, A58
Zhao, B., Li, Z.-Y., Nakamura, F., Krasnopolsky, R., & Shang, H. 2011, ApJ,
  742, 10
```